Zagazig University
Faculty of Engineering
Structural Engineering Department

Utilizing Pile Integrity Test in testing shallow foundation cracking

A Thesis

Submitted to Faculty of Engineering

Zagazig University

For

Master of Science

in

Structural Engineering (MSC)

By

Abdalla Eliwa Abdalla Elmesallmay

(B. Sc. in Civil Engineering, 2001)

Prof. Tarek Nageeb Salem

Professor of Geotechnical Engineering,
Structural Engineering Department,
Faculty of Engineering,
Zagazig University.

Prof. Atef Eraky Bakry

Professor of Structural Analysis,
Structural Engineering Department,
Faculty of Engineering,
Zagazig University.

2023

DEDICATION

To the most loving and caring mother;

To the most precious father;

To my lovely wife,

To my daughters;

To my wonderful brothers and sister;

I DEDICATE THIS WORK

ACKNOWLEDGMENTS

I would like to express my sincere appreciation and gratitude to Prof. Dr. **Tarek Nageeb,** Professors of soil mechanics and foundation and Prof. Dr. **Atef Eraky,** Professor of Structural Analysis, Structural Engineering Department, faculty of engineering, Zagazig University, for giving me the opportunity to pursue this degree under their guidance and support that enriched my experiences professionally and personally. Their timely appreciation of my work was a great source of encouragement. Grateful Thanks of their endless support throughout this work. Their expertise in geotechnical and structural engineering improved my research skills and prepared me for future challenges. Finally, I express my deepest appreciation and thanks to my great mother, my father and my wife for their patience, support, and great encouragement.

ABSTRACT

Pile integrity test is non-destructive test that can assess the integrity and soundness of the reinforced concrete pile body. Non-destructive testing is superior over any other test for the fact that the structural element body is kept intact as before the testing. Pile integrity test idea starts with inducing an internal body wave and tracing the wave propagation along the pile body in an effort to pin-point the zone(s) of defects. More progress in the test allowed for identifying the type of defect. The idea of using wave propagation to assess the pile body integrity is further extended to identify the defects and/or cracks in shallow foundations.

The research objectives are employing the pile integrity test theory in detecting damages within shallow foundations, extending the test to theoretically locate cracks, and damaged zones within shallow foundations, interpreting pile integrity test signals and graphs in locating the cracks and damaged zones in footings and proposing procedure for correcting the readings of the pile integrity test to simulate the damage detection in reinforced concrete footings. The analysis is performed using the finite element software ADINA in modeling the stress wave propagation in piles as prismatic members first. Extending the numerical approach to circular footings, is a further step from the long prismatic member (pile) and the final intended shape of circular surface footings. Compiling a performance database and categorize waves based on their footing material properties and dimensions. Studying the wave propagation in piles and extending the study to footings of different shapes under cyclic force with sinusoidal function, and impact function. Studying the wave propagation in both intact and defected piles and

footings. Providing a perspective for a compatible wave analysis of both intact and cracked piles, and extending the case for circular shallow footings in both cases of intact and defected footing bodies.

TABLE OF CONTENTS

List of Figures

List of Tables

List of notations

SHM	Structure health monitoring
NDT	Non-destructive test
NDE	Non-destructive evaluation
ADINA	Automatic Dynamic Incremental Non-linear Analysis
AUI	ADINA user interface
CM	Condition Monitoring
PIT	Pile integrity test
IR	Impulse Response
TDR	Transient Dynamic Response
SE	Sonic Echo
IL	Impedance Log
IE	Impact Echo
CSL	Cross-hole Sonic Logging
PS	Parallel Seismic
HHT	The Hilber-Hughes-Taylor technique
CWT	Continuous Wavelet Transforms
FT	Fourier Transform
QC	Quality Control
QA	Quality Assurance
CPT	Cone Penetration Test
SCPT	Seismic Cone Penetration Test
FEM	Finite Element Method

ADINA	Automatic Dynamic Incremental Non-linear Analysis
AUI	ADINA User Interface

Chapter One

Introduction

Chapter (1)

Introduction

1-1 General

It is widely accepted that maintenance of engineering structures is important to ensure structural integrity and safety. This is particularly relevant to civil engineering and transportation. A variety of different Nondestructive Testing and Evaluation (NDT/E) methods have been developed for damage detection. NDT/E techniques are often limited to single-point measurements and require scanning when large areas need to be monitored. In recent years there have been a range of new damage detection techniques and sensing technologies. These methods allow for global, online monitoring of large structures and fall into the area of Structural Health Monitoring (SHM). They are capable of achieving continuous monitoring for damage involving the application of new sensors.

Damage monitoring systems, which often use advanced sensor technologies, are concerned with a new design philosophy. Actuators, sensors, and signal processing are integrated to offer progress in this area. SHM involves integrating sensors and actuators, possibly smart materials, data transmission and computational power within a structure in order to detect, localize, assess and predict damage which can be a cause of structure malfunction in the present or in the future. A typical SHM system is associated with an online global damage identification in structures; such systems are most often applied in civil engineering. Although SHM systems utilize NDT/E methods as tools, there are many differences in SHM and NDT/E operation principles. NDT/E techniques are commonly applied offline and locally in regions of expected damage

while SHM methods should provide real time monitoring of a whole structure during its operation.

SHM is a successive step in the evolution of structure diagnostics, which historically evolved from the damage detection concept implemented in the form of Condition Monitoring (CM) systems. CM systems should be capable of detecting damage based on a global assessment of technical structures during their operation. SHM is expected to go further by the ability of detecting damages in early stages of their development or, in an ideal case, of predicting their occurrence before they really take place.

1-2 Problem Statement

Shallow foundations and piles are concrete structural elements, their executions accompanied with site conditions and problems. These conditions always lead to defects in the concrete casting like honeycombing, bulges and cracks. Lack of quality control and other reasons may cause these flaws. Monitoring these defects may be done by using sub-sonic waves. PIT is an instrument that induces these waves and monitors and analyzes them.

The research objective is to utilize sub-sonic waves at shallow foundation to monitor cracks or defects through modeling several scenarios. Utilizing PIT in shallow foundation is relatively low-cost methodology to guarantee the concrete health.

1-3 Research Objectives

The research objectives can be stated as follows:

1- Employing the pile integrity test theory in detecting damages within shallow foundations.

2- Extending the test to theoretically locate cracks, and damaged zones within shallow foundations.
3- Interpreting pile integrity test signals and graphs in locating the cracks and damaged zones in footings.
4- Proposing procedure for correcting the readings of the pile integrity test to simulate the damage detection in reinforced concrete footings.

1-4 Thesis Organization

The thesis is composed of five chapters along with a list of references and an Arabic summary.

- Chapter (One) presents general introduction, problem statement, research objectives, and thesis organization.
- Chapter (Two) presents review of the researches performed on pile integrity tests numerically, analytically, practically and on structural health monitoring in general.
- Chapter (Three) presents employing elastic wave propagation theory and employing numerical modeling by ADINA software.
- Chapter (Four) presents results and discussions for modeling of defect scenarios in piles and scenarios in shallow foundations.
- Chapter (Five) presents the main conclusions obtained from the study results and provides recommendations for further researches.

Chapter Two

Literature Review

Chapter Two

Literature Review

2.1 Introduction

The importance of assessing the construction quality of a pile foundation has long been recognized. To achieve this goal, various kinds of destructive and nondestructive tests were developed. In this aspect, nondestructive testing (NDT) was considered to possess high potential for application because it is featured as cost-effective, damage-free, time-saving, and thus can cover the whole population to avoid the disadvantages of sampling (Baker et al., 1991). The primary goal of carrying out a nondestructive test on a pile is the acquisition of the geometric configuration of the pile. This information, describing the detailed geometry of the pile and the embedded defects if they exist, can first be used to evaluate the integrity of the pile and then be served as the input of a subsequent nonlinear finite element analysis to estimate the pile capacity (or the ultimate strength) of the pile. This philosophy exposes the vast space that NDT can apply in the future. However, all these potential applications rely on the success of NDT in obtaining the detailed geometry of the intact or defective piles (Liao and Roesset, 1997a).

Many researchers have been working on the NDT of piles. Most of the tests can be classified into two categories, (1) reflection and (2) direct transmission methods. Tests categorized in reflection methods are:

- Impulse Response (IR) (Davis, 2003; Finno and Gassman, 1998) or Transient Dynamic Response (TDR) (ASTM-D-5882 2004; Dav and Dunn, 1974).

- Sonic Echo (SE) (Rausche et al., 1991).
- Impedance Log (IL) (Paquet, 1991; Rix et al., 1993).
- Impact Echo (IE) (Lin et al., 1997; Sadri and Afshin, 2003).

Cases where tests as categorized in direct transmission methods:

- Cross-hole Sonic Logging (CSL).
- Parallel Seismic (PS) (Olson et al., 1995).
- Štrukelj et al., (2009) introduced a monitoring methodology where sensors are installed inside the pile body to measure the pile strain under dynamic load. The results of the experiment are compared with a numerical model conducted by PLAXIS software.
- Trauner (2012) studied the behavior of reinforced concrete pile inside a soil domain under dynamic load. Sensors are installed on the steel reinforcement bars to measure the strain of the pile.
- Furthermore, verification is conducted with a real PIT carried out on the field. Ding et al., (2011) studied the PIT wave propagation in a tube section pile numerically. Models are carried out with different wall thickness and different elastic moduli.
- Niederleithinger (2006) and (2008) described the CEFIT software to simulate the PIT and the acoustic wave through the pile and the soil.
- Zhang et al., (2010) used ANNs software to simulate the PIT with neural network technique.
- Warrington and Wynn (2000) studied the difference between the software MAPLE, ANSYS and WEAP, in simulating wave equation through concrete piles.
- Li, (2019) studied large-diameter pipe pile embedded in inhomogeneous soil to investigate the torsional dynamic response,

and presented verification of the frequency-domain analytical solution.

- Wu et al., (2019) study the longitudinal vibration of a pile with changeable sectional acoustic impedance under arbitrary external stimulation. The Laplace transform is used to find the analytical solution of the transfer function, and then the residue technique of inverse Laplace transformation is used to solve the corresponding impulse response function. The analytical solution of response at pile top may be found by convolution computation using the impulse response function, which overcomes the limit of earlier analytical solutions due to defined time-harmonic load.
- Li and Gao, (2019) introduced better approach for describing the vertical vibration of a pipe pile while taking into account the layered characteristics and building disturbance impact of both the outer and inner soils for various pile specifications and soil radial inhomogeneity conditions, the impacts of the inner soil on the dynamic response of the pipe pile were explored. The theoretical model's accuracy was confirmed by comparing the outcomes of field measurements.

In reflection methods, the force to introduce a disturbance to a pile and the receiver to collect the response of the pile are basically applied at the pile head. Whereas in direct transmission methods the receiver is placed at intervals in a tube or borehole which must be cored or drilled before testing. Therefore, reflection methods are in general faster and more cost-effective. However, direct transmission methods can obtain the information in a more direct way and they can be applied to piles with much larger length. Among the reflection methods, Lin et al. (1997) used

the IE tests to successfully detect the lengths of piles and the depths of the embedded necks.

Using the finite element method, Liao and Roesset (1997b) developed one, two, and three-dimensional models to simulate the IR test for intact piles. A series of parametric studies were carried out to demonstrate the capabilities of this method in determining the lengths and cross-sectional areas of intact piles under various kinds of soil conditions. The numerical models of IR tests were later extended to study piles with axisymmetric irregularities such as necks and bulges. The results indicated that by analyzing the mechanical admittance (or mobility) curves, the depth and length of the necks (or bulges) can be determined in good precision. However, the methodology to determine the widths of the defects seems to remain pending.

2.2 Review On Piles Damage Detection Through Analytical Methods

Newly constructed piles are routinely evaluated using a low strain integrity test to assess their integrity as part of a pile foundation quality control program. A mathematical model developed by ***Nazir and El Hussein***[1] integrates soil effects and is based on numerical solution of the wave equation. This model takes into account the impacts of soil resistance on the stress wave that propagates through the pile body as a result of hammer impact. The numerical analysis is carried out with the help of a computer software that was created based on pile integrity test mathematical modeling. The produced velocity values are found to be quite comparable to in-situ test findings when the simulation software output is compared to real pile integrity test results. A new technique is

demonstrated that uses the known model to identify pile integrity test limits.

The effects of soil friction at the perimeter of the pile and soil resistance at the tip of the pile created during the low strain integrity test technique are quantitatively analyzed. The mathematical model is based on the fundamental wave equation being amended to include soil resistance at the pile surface and pile toe. The skin friction is thought to be proportional to pile displacement, whereas soil resistance at the pile toe is thought to be produced by a change in impedance as well as the dynamic response at the pile tip. The new technique of analysis produced findings that were equivalent to those obtained from in-situ low-strain integrity tests leading to the introduction of a novel approach for evaluating low strain integrity tests. Based on pile and subsurface soil conditions, as well as the sensitivity of the PIT tester, this approach may be utilized to assess test limits. The sensitivity of the PIT equipment must be determined in order to determine if the model predicted values at the pile toe may be recognized by the equipment or not.

Wang et al. [2] examined the dynamic longitudinal interaction between the soil-pile in viscous layered soils by modeling the surrounding soil as a three-dimensional axisymmetric continuum taking into account its wave impact. Since the soil is stratified and viscoelastic, it is believed that the pile is vertical, elastic, and of uniform cross-section. It is theoretically examined how a pile's longitudinal vibration changes with arbitrary weight on layers of viscous damping soil. The problem in frequency domain can be resolved by applying the Laplace transform.

A definitive solution to the issue of longitudinal vibrations in a finite pile sitting on an elastic stratum with changing section impedance is established utilizing the δ function, according to ***Gao et al.***[3]. The characteristic equation for the issue is constructed by decoupling the variables and employing the boundary and continuity conditions of the pile-soil system, after which the appropriate eigenvalues are calculated numerically. The analytical answer for a pile exposed to time-domain steady sinusoidal stimulation is then derived. The amplitude-frequency charts are evaluated come to certain conclusions. The notion of superposition is used to arrive at an analytical solution for a pile exposed to transient stimulation in the time domain. The features of signals reflected off a defect are then investigated in a parametric analysis, which yields many key implications for practical defect identification. The theoretical and measured curves are then compared, and two engineering projects are discussed. The following equation expresses the velocity response of the pile top:

$$u(0,\tilde{t}) = \frac{2}{p_n}\frac{Q_{max}}{SE_1}T_C C_1 \left\{\left[F_{1n}^{`}\frac{r_2^{`} e^{r_2^{`}\tilde{t}^{`}} - r_2^{`} e^{r_2^{`}\tilde{t}^{`}}}{\Delta r} + F_{2n}^{`}\frac{e^{r_2^{`}\tilde{t}^{`}} - e^{r_2^{`}\tilde{t}^{`}}}{\Delta r}\right].a_3 + F_{2n}^{`}.Sin(a_3\tilde{t}) - a_3F_{2n}^{`}.Cos(a_3\tilde{t})\right\} \quad (2.1)$$

A definite problem describing the excited vibration of a pile with variable section impedance subjected to steady sinusoidal and transient excitations at its top was established using generalized functions, taking into account the impact of the surrounding soil and the position of the pile tip on an elastic stratum. Then, a theory of vibration and detection in pile foundations was developed using the analytical solution as a foundation. The displacement response and the excitation frequency caused by a

continuous sinusoidal stimulation at the pile top have theoretical formulations for their amplitude-frequency and phase-frequency relationships. Using the resultant analytical solution, the relevant curves were numerically generated, and the impacts of the defect factors on these curves were examined. The findings demonstrate a strong correlation between the defect features and the amplitude-frequency curve. These findings led to the suggestion of utilizing the amplitude-frequency curve to determine the faulty features.

The parallel seismic (PS) method, a nondestructive test method for finding reinforced concrete pile faults, was introduced by ***Wu et al.*** [4]. The technique may be used to find serious pile faults in both existing piles supporting a superstructure and new piles. In this study, a linked model of a fault pile and fictional soil pile is created while taking into account the three-dimensional influence of the surrounding layered soil. The dynamic reaction of the soil surrounding and beneath the pile is addressed analytically. The impacts of pile defect and layered soil condition on the dynamic response of nearby soil are then investigated using the created solution. The findings of a parametric analysis are used to create realistic guidelines for the parallel seismic method's use in pile integrity testing.

The ring-soil pile theory (RSPT) and an amended impedance function transfer method (AIFTM), are proposed by ***Gao and co.*** [5] as models of rigid pile-soil interaction that take into account the interaction at the variable-section interface of a pile with the surrounding soil. These models take into account the displacement and stress continuity conditions at the pile-soil interface. To determine the impedance function at the pile top, the interactions between nearby three-dimensional soil layers are condensed into uniformly distributed Voigt models. The

velocity response at the top of the pile in response to brief stimulation is calculated using an inverse Fourier transform. An engineering example is provided to demonstrate the logic of the suggested fix. The answer can be reduced to other previously suggested solutions for certain pile shaft geometrical characteristics. The suggested approach is contrasted with one that ignores the interaction between the pile's variable-section interface and the surrounding soil, and the combined impacts of the relevant pile-soil characteristics and the interaction there are also examined. The following equation expresses displacement at k^{th} segment in pile

$$W_k = \left[\sum_{m=1}^{\infty} \frac{T_{1km}\, C_{km}^{`}\, Cos\left(B_{km}\, Z_k^{`} - \theta_{km}\right)}{\left(D_{km} - C_{km}^{`}\right) T_{3km}} + Sin\left(P_k\, Z_k^{`}\right)\right] M_k + \left[\sum_{m=1}^{\infty} \frac{T_{3km}\, C_{km}^{`}\, Cos\left(B_{km}\, Z_k^{`} - \theta_{km}\right)}{\left(D_{km} - C_{km}^{`}\right) T_{3km}} + Cos\left(P_k\, Z_k^{`}\right)\right] N_k \quad (2.2)$$

A uniformly distributed Voigt model is used to represent the interactions between three-dimensional soil layers, and an analytical solution is presented for the excited vibration of a pile with a changing cross section. An engineering example is provided to demonstrate the logic of the suggested fix. The solution put forward in this work reduces to the appropriate classical solutions for particular values of the variable-section segment's radius. The burial depth of the defect for a pile with a neck is more accurately estimated from the curve calculated using the proposed model, which takes into account the interaction at the pile's variable-section interface with the surrounding soil, than it is from a curve calculated using a model that does not.

2.3 Review on Piles Damage Detection Through Numerical Methods

Low-strain reflected wave technique is one of the most widely utilized dynamic pile test technologies and is increasingly employed in

pile integrity testing. Currently, field testing is only used for basic defect discrimination. However, it lacks knowledge of the stress reflection law of various degrees of defects, particularly that of quantitative defect analysis. ***Wang and others*** [9] tackled the issue, discrepancies in the reflected waves from various faulty piles are studied, and the finite element approach is used to simulate scenarios with various degrees of segregation. According to the theory that the velocity-time curve is consistent, which combines the defect characteristics of the ratio between the reflected wave peak and the incident wave peak and the concrete modulus between the segregation section and the degree of pile concrete segregation was quantified and analyzed. The development of the finite element approach will provide crucial direction for engineering applications as figure (2-1) shows.

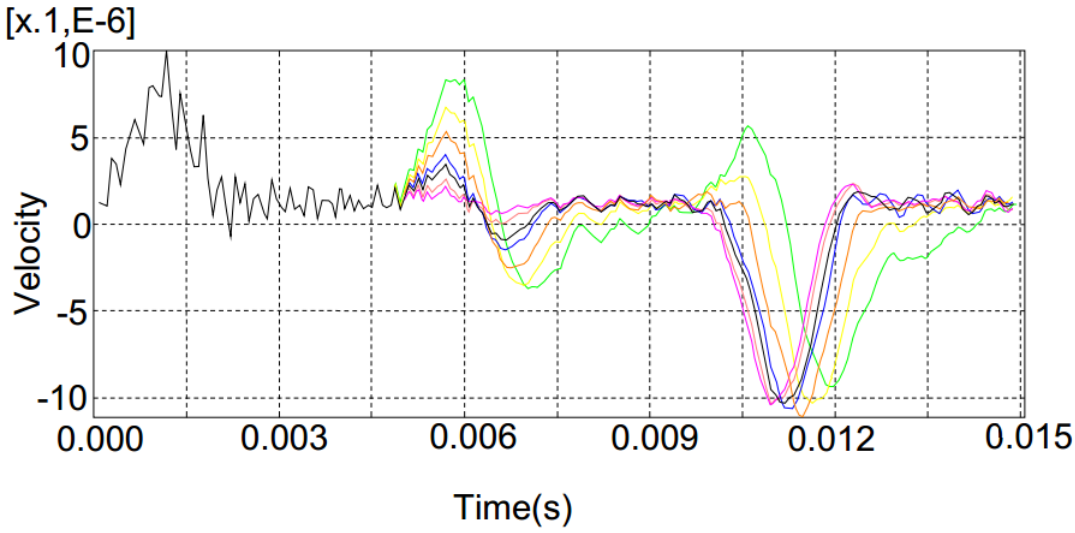

Figure (2.1): Velocity versus Time for Different Piles' Moduli. [9]

The criteria for finite element computations can still be met by ignoring the impacts of soil resistance. Incident wave phase of the distinctive reflected wave of the pile with necking or segregation is comparable to the integral pile. However, necking has a smoother waveform than segregation. With an increase in necking length, defect waveform positive and negative pulse separation and pile reflection

arrival delay will happen. When compared to necking pile, segregation pile doesn't appear to be in a comparable scenario as positive and negative pluses separation, which is a clear distinguishing feature for both faulty heaps. Since the wave impedance falls at the necking defect interface, the reflected waveform is identical to the incident waveform there. The reflected waveform is not affected by the necking's position fluctuation. Rather than density, the pile's modulus of segregation is a clear primary element that will affect the velocity vs time curve.

To mimic necking flaws with variable extents, locations, lengths, etc., ***Zegen et al.*** [10] developed a finite element model of several types of necking piles. The velocity time history curve's effects on various variables are examined. The typical reflected waveform at the necking defects is consistent with the incident waveform because the wave impedance diminishes at the interface of the defects. Changes in the necking location have minimal impact on the reflected waveform from the bottom. The distinctive reflected wave at the shallow pile is easily overrun by the incident if the pulse width is too broad, which makes it difficult to see the waveform from the bottom if it is too short. The distinctive reflection will lengthen with the necking, and when the length approaches a specific point, the reflected wave from the severe necking flaws will overlap the reflection from the bottom. When the radius is reduced to a certain point, the stress wave will only reflect between the top of the pile and the faults, making it difficult to see the distinctive reflection from the bottom.

In order to replicate non-destructive testing utilizing the pile integrity test (PIT), ***Cosic and others*** [11] developed a discrete numerical 2D and 3D solid pile model with a discontinuity and faults. Reducing the specific finite elements and the elastic modulus of concrete allowed for

modeling of the pile discontinuities and faults. The Hilber-Hughes-Taylor [HHT] technique in the time domain was used to numerically integrate and analyze the pile's wave-propagation response. The initial formulation of the idea of a system-response analysis was based on the fusion of separate reflectograms into a reflectogram surface, which is produced in a 3D cylindrical coordinate system. Reflectogram surfaces provided for a deeper knowledge of wave propagation based on velocity than is often possible with conventional, one-dimensional reflectograms. There is a definite variation in the reflectograms depending on where the measurement point is located, and changes in the velocity responses on the reflectogram, moving from a positive to a negative value, point to the locations of discontinuities and flaws in the discrete 3D pile model. The following reflectogram typological models are described in the study as pile-head defect, defect in the middle of the pile length or a reduced modulus of elasticity in the middle of the pile length, defect in the pile-base or a reduced modulus of elasticity in the pile-base zone, and reduced modulus of elasticity in the pile-head zone.

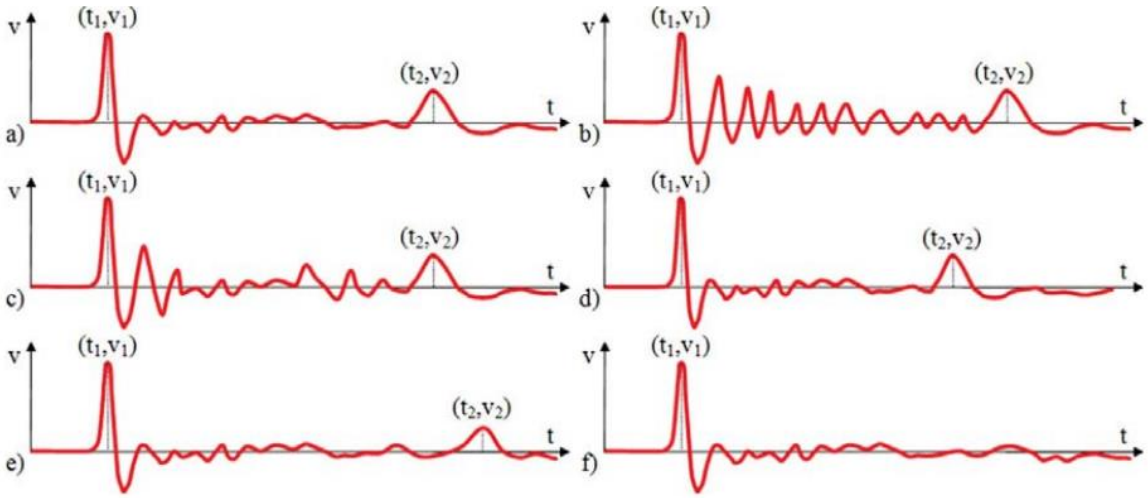

Figure (2.2): Reflectograms: a) "Normal" Pile Length without Discontinuities and Defects, b) Problem with the Pile Head, c) Discontinuity in Impedance Reduction, d) Pile Length is Shorter Than Designed, e)

Pile Length is Longer than Designed, f) There Is a Deviation or There Is a Lack of Clear Wave Reflection in the Pile Toe. [11]

In order to replicate non-destructive testing utilizing the pile integrity test (PIT), discrete numerical 2D and 3D solid pile models with a discontinuity and faults were developed. By lowering the specified finite elements and applying the Staged Deterioration Analysis (SDA), the pile discontinuities and faults were simulated. The lowering of the elastic modulus in particular zones introduces the influence of the pile concrete quality degradation. The Hilber-Hughes-Taylor [HHT] technique in the time domain was used to numerically integrate and analyze the pile's wave-propagation response.

The initial formulation of the notion of system response analysis relied on the fusion of distinct reflectograms into a reflectogram surface, which is produced in a 3D cylindrical coordinate system. The asymmetric pile toe, asymmetric pile-head defect, asymmetric reduction of cross-section in the middle of the pile length, asymmetric reduction of cross-section in two locations along the pile length, significantly degraded pile along its full length, different elastic modulus in the pile-toe zone, and different elastic modulus. There is a distinct difference between the reflectograms based on where the measurement points are located, and shifting the response velocity on the reflectogram from positive to negative values reveals the locations of discontinuities and flaws in the discrete 3D pile model. The following typological reflectogram models are described in the study: without discontinuities and defects, pile-head defect, defect in the middle of the pile length or a reduced modulus of elasticity in the middle of the pile length, defect in the pile-base zone or a reduced modulus of elasticity in the pile-base zone, and a reduced

modulus of elasticity in the pile-head zone. The next stage of researching numerical simulations of the PIT is the detection of cracks in the pile.

Despite its impact on test outcome, the impacts of surrounding soil on pile integrity test findings are still not fully characterized. Due to the effects of soil damping, it is typically challenging to determine the stability of piles socketed in hard soil strata. During a pile integrity test, a method for estimating the impacts of soil damping on stress wave force and velocity data is described. ***El Hussien and Nazir***[12] developed a theoretical model using the wave equation's numerical solution. The effects of soil resistance on wave propagation in piles are included in this model. Results from the proposed model were compared to those from PIT-S software, which simulates the propagation of low strain waves in piles under the assumption that the pile is cast in extremely dense granular soil. The produced Force-Velocity curves were found to be comparable when comparing the two approaches, however some variances were seen near the pile toe because of the various methods employed for estimating soil response. In addition, the model's output findings were contrasted with those of actual in-situ pile integrity tests and PIT-S. In comparison to PIT-S software, the model demonstrated superior prediction of the received pile toe signal.

Hou et al. [13] simulated low-strain testing of piles, based on the 3D dynamic finite element method to describe the integrity of a foundation with faulty piles. The integrate piles' velocity-time curve is derived. Between modeling findings and the pile testing curve, there was considerable consistency. Research on the low-strain dynamic effect of faulty piles is based on the integrate piles analysis. The fault is specifically the difference spread cervical position, different necking positions, and different thickness of segregation. The simulation was used

to forecast damaged piles and to diagnose their quality, providing a theoretical foundation for field experiments to determine the precise locations of flaws and the extent of their harm.

The ABAQUS/Explicit finite element program is used to simulate the low strain reflected wave approach to various types of faulty piles. The hammer-pile-soil model has been established. In the transient exciting force, the velocity-time curve of the pile head is retrieved. The actual data and the simulation exhibit good agreement. The reliability of the simulation has been confirmed. Then, by modeling the defective piles using controlling factors, the placements of the defective piles are verified. In order to give a theoretical foundation for the concrete position confirmation and damage degree of a faulty pile in pile field testing, this study anticipates numerous types of defective heaps and diagnoses their quality. Additionally, it may be used to simulate analyses of the material, cross-sectional area, and various positions of segregation, as well as the thickness and cross-sectional area of distributed cervical and necking.

2.4 Review on Piles Damage Detection Through Practical Methods

For many years, non-destructive evaluation methods have been used to offer pile construction quality control. To assess the lengths and integrity of freshly built piles, low strain pile integrity test techniques have been deployed. Defects and unwanted background noise impair the signals used to assess the integrity of piles that are obtained from receivers on pile heads. ***Ni et al.***[15] used the Continuous Wavelet Transforms [CWT] approach with time-frequency distribution to improve the testing signal's features and increase identification capacity. The in-situ examinations of the drilled shaft show that testing signals might be simultaneously exhibited in the time-frequency domain and then be

investigated by CWT at each and every occasion. CWT can improve the signal and increase the amount of viewable data. Even for long drilled shafts, it has been demonstrated that CWT and Sonic Echo [SE] technologies may be used to visually assess and swiftly detect the pile integrity.

A mathematical method and tool for signal processing, wavelet analysis enables the signal to be examined in the wavelet time-frequency domain. This is a novel way of signal analysis for the SE method. The findings indicate that such a method could offer a more thorough way of examining the signal. The results that may be derived are as follows: The pile tip and faults that are visible in the time-frequency domain of CWT may be clearly seen using the wavelet analysis of the SE technique. Thus, compared to previous techniques, SE testing data may be evaluated more quickly, accurately, and reliably. In the past, the conventional Fourier Transform (FT) approach could be used to show and evaluate the time and frequency connections of signals. Now that CWT is being used, the SE testing signal may be concurrently shown in the time-frequency domain. In the whole signal, the frequency change may be pinpointed at any moment. Even for long drilled shafts, it has been demonstrated that it is possible to combine CWT and SE approaches to rapidly and readily comprehend and determine the pile integrity picture.

It is not clear how the pile-soil interaction will affect the Pile Integrity Test (PIT). However, casting heaps on hard soil layers may provide contradictory results. In pile integrity testing, the soil in which the pile is embedded attenuates the stress wave's propagation. A theoretical model that takes into account the effects of pile material and soil damping on wave propagation in the pile body was developed by ***Hussien and Nazir*** [16] using the numerical solution of the wave equation.

When model findings were compared to actual in-situ PIT data, it was discovered that there was a good degree of resemblance. The dampening effects on the PIT findings are also evaluated using the model. After integrating soil resistance factors, the impacts of the pile material and the soil on skin friction and the influence of the soil on the pile toe were evaluated using a numerical solution of the wave equation.

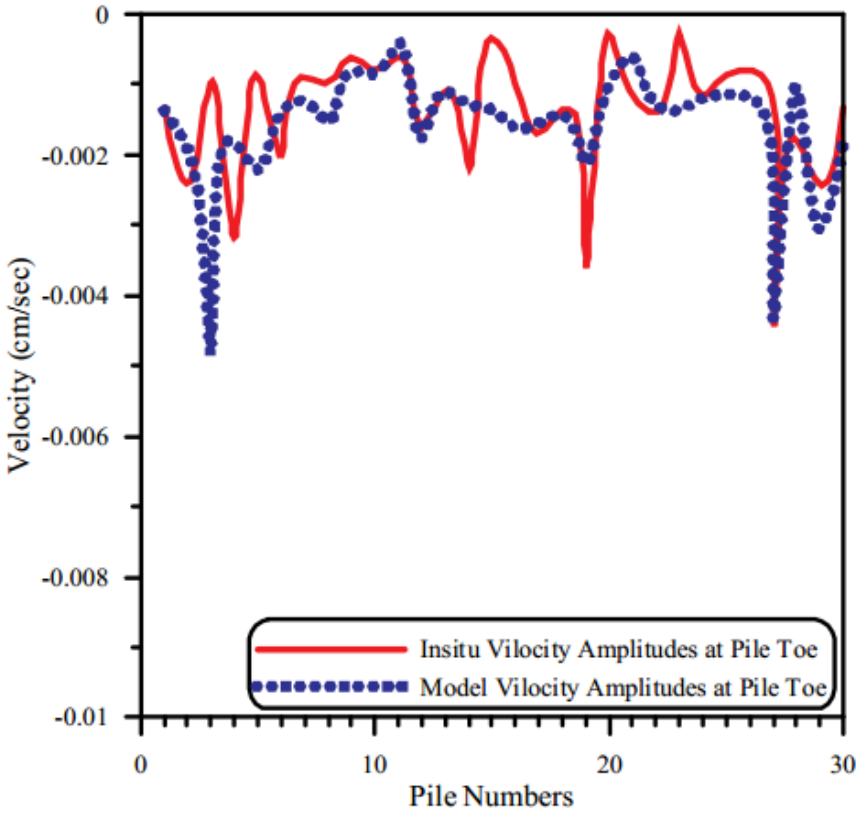

Figure (2.3): Velocity Amplitudes Produced from Insitu PIT and the Model. [16]

The mathematical model is based on the fundamental wave equation being modified to include pile material damping and soil resistance at the pile surface and the pile toe. It is thought that skin friction is proportional to pile displacement. This presumption is seen to be more appropriate for dynamic loading since it allows for the quantification of tiny, instantaneous mobilized frictional forces. Results from the model were found to be equivalent to those from actual in-situ

tests. Based on the pile and subsurface soil conditions, the PIT tester sensitivity, and this model, the PIT test limits may be assessed.

High strains are placed on driven piles during installation. Therefore, it's crucial to maintain reasonable tensions at the toe and along the pile shaft in order to avoid damage. Dynamic monitoring has been utilized for many years to assess installation loads as well as look for structural damage in test piles. Over thirty years ago, the Beta Method [ß-Method] for assessment of the location and scope of a potential harm was established, and it has proved successful as a Quality Control (QC) and Quality Assurance (QA) tool. The ß-Method also provides a grading scale that converts the automatically calculated ß-number into a useful pile integrity evaluation tool, aiding in the process of pile rejection or acceptance. This algorithm's dependability has been demonstrated by a large number of tested piles. The conventional ß-Method is less successful in detecting damage close to the pile toe because to high toe resistance effects and/or stress wave reflections. This was one shortcoming of the ß-method. Therefore, in the past, the testing engineer determined near-toe damage by reviewing the pile toe compressive stresses over the course of the monitored driving history as well as the strength and stiffness of the soil response from the pile toe, in addition to visually inspecting the dynamic monitoring data. This method has now been automated and tested using historical data. ***Likins et al.*** [17] reviewed the current techniques for calculating pile stress and damage before introducing the new technique and demonstrating its efficacy with examples drawn from measurements of both concrete and steel piles.

Because it gives construction experts a thorough evaluation of a foundation's geotechnical and structural suitability, dynamic pile monitoring in accordance with the Case Approach has been widely

accepted as a quality control and assurance method. Rational judgments about the acceptance or rejection of a pile are based on the predicted bearing capacity, pile stresses, hammer performance, and the ß-integrity factor taken together. Over the course of the next more than three decades, a large number of independent engineers have employed the ß-method to detect damaged piles. The ß-Method was created for the detection and quantification of damage along the pile shaft. The correctness of the first suggestions drawn from theory was then independently tested by extraction for major damage. To identify possible damage at any site underneath this point of measurement, the ß-Method just needs instrumentation close to the pile head. Since it may be used for any driven pile, even after the fact, and prevents additional equipment from becoming permanently lodged in the pile, this single point of measurement makes instrumentation reusable and consequently cost-effective. Using remote testing technologies will result in more savings. The ß-Method also has the benefit of being applicable to any pile with a uniform cross section, including steel and concrete piles, which accounts for the great majority of driven piles.

The refit of existing buildings is hampered by a lack of knowledge regarding the depth of a foundation part. Non-destructive geophysical techniques could be an affordable tool for accurately determining the depth of foundational components. The Low Strain Dynamic Pile Tests methodology, also known as Pile Integrity Testing [PIT], is one such technique that has recently been utilized to gauge the depth of existing foundations. The depth and integrity of foundation components are evaluated using the PIT in two case studies that are presented through ***Souza and others***[18] research. The communications towers were of the self-supporting variety, and their foundations were made of a root-pile

injected with sand and a caisson on sandy clay. Considerations for site preparation and signal acquisition are addressed, and the resulting wave signals are analyzed.

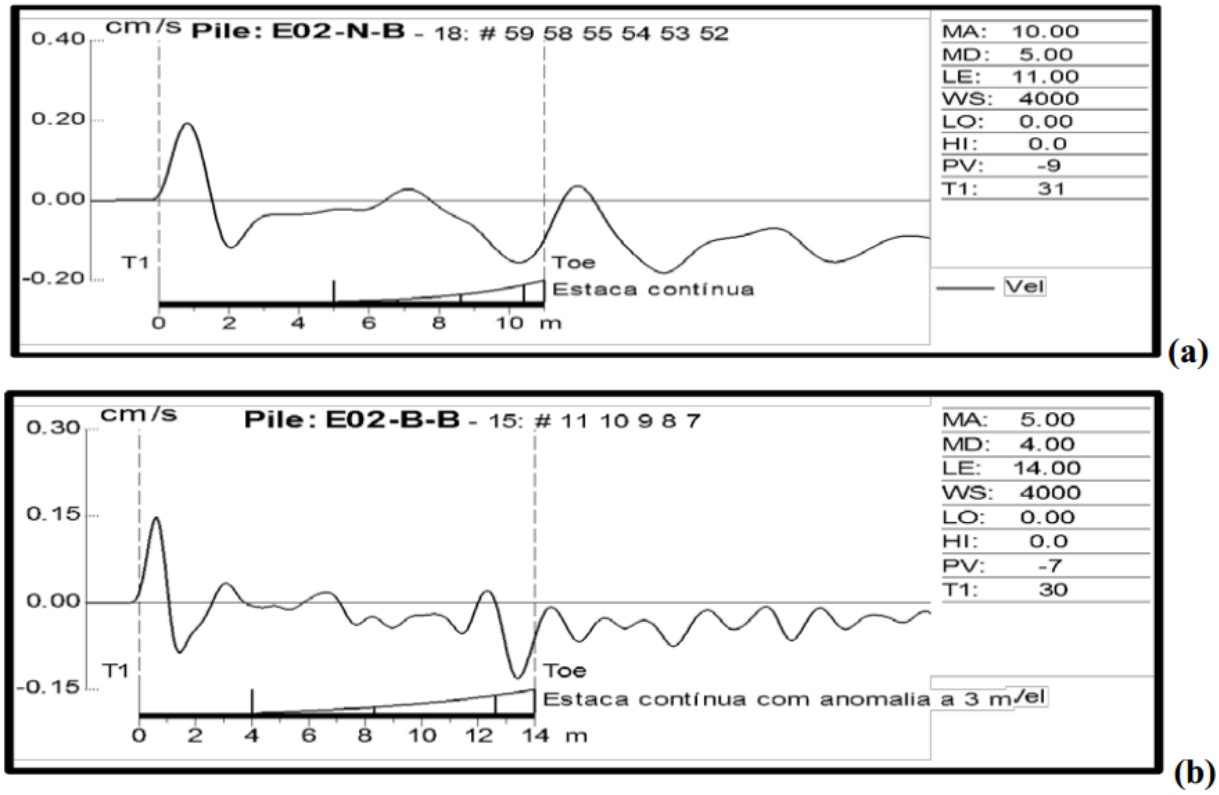

Figure (2.4) Average PIT-W signals acquired: (a) on the root-pile shaft, and (b) on the top of the block [18]

The most frequent question regarding piles is whether or not their integrity is suitable. The appropriate detection of a small flaw under a significant defect is another issue that hasn't often been brought up. In order to conduct this investigation, ***Promputthangkoon et al.*** [19] modeled concrete piles with dimensions of 0.15 by 0.15 by 5.00 m were built, with two flaws placed purposefully at 2.50 and 3.50 m from the pile top. The second flaw was modified such that the values ranged from 95, 90, 85, 80, 65, 50, 35, and 20%, but the first defect was made to have a constant

value of 40%. These flaws were found using a pile integrity testing device, and the findings were compared to the ones that were really made. To test if skin friction might alter the signals, tests were done with the piles both above and below the ground. The average measured values for the first flaw were discovered to be, respectively, 76% and 89% greater than those of the real faults. When evaluating the signals from a report, engineers should keep this key issue in mind. For instance, a stated flaw is likely less significant than the damage to the pile. In the instance of the second flaw, the outcomes showed that the pile should be acceptable if an A value is 89% and above. If it is less than 89%, however, further pile integrity testing should be done to clarify the outcome.

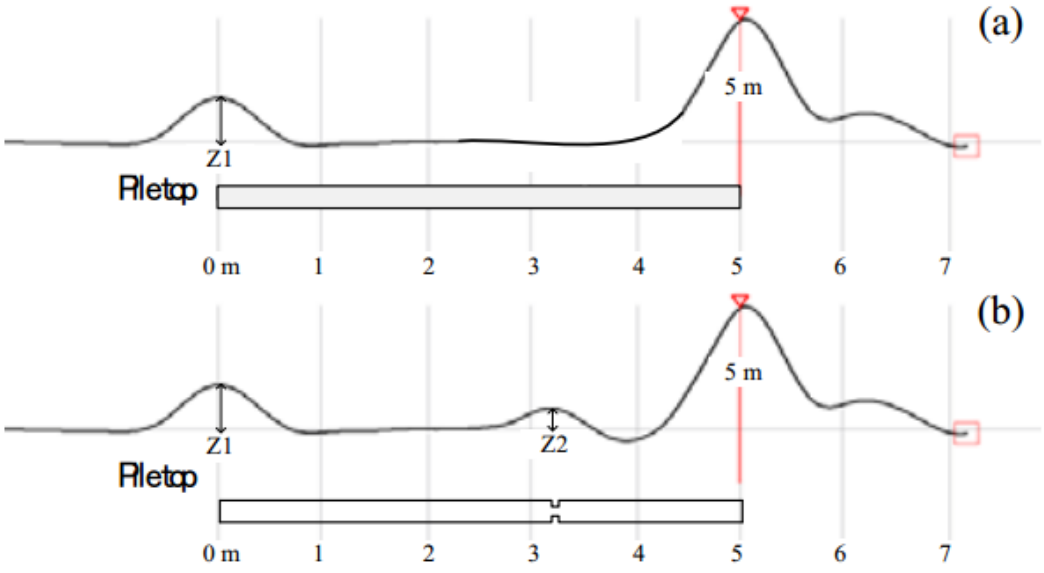

Figure (2.5) Examples of velocity record obtained from the machine employed (a) normal pile (b) defected pile. [19]

Two flaws, which were placed at 2.50 and 3.50 m from the pile top, were built into concrete piles that were 0.15 by 0.15 m and 5.00 m long. A value of 40% was achieved by creating the upper flaw. Lower faults have been altered to have values between 95, 90, 85, 80, 65, 50, 35,

and 20%. To assess the flaws, the pile integrity testing apparatus model PET was used. The integrity test was conducted with the pile horizontally lying in the air and with the pile sunk 30 cm below earth. Overall, it was found that the measured values for the first defect's piles in the air and underground are, respectively, 76% and 89% greater than those of the real ones. This implies that it's important to understand the distinction between a report and, most likely, the real harm caused in the pile. In the instance of the second flaw, the pile may be acceptable if the indications indicate that a value is around 89% or higher. However, if a number is less than 89%, it should be disregarded, and additional integrity tests should be conducted to determine the pile's integrity.

Chapter Three

Theory and Modeling

Chapter Three

Theory and Modeling

3.1 Elastic Wave Propagation

Numerical simulations are frequently used to predict the possible wave field, providing an insight into mechanisms that drive the wave interaction with structural features. This enables employment of simulation methods in the design, operation, and improvement of Structural Health Monitoring (SHM), Non-Destructive Test and Non-Destructive Evaluation (NDT/NDE) systems as a mean of optimizing the system's characteristics, as well as a part of the system to support damage detection and localization. At the design stage of a monitoring system, numerical simulation helps to adjust the settings, choose optimal sensors' positions or examine the system's response for various damage configurations. This may be performed virtually, reducing the number of test samples and physical experiments, and minimizing the time required for the monitoring system design. During the operation phase, the simulation may be employed as a part of the system providing a virtual baseline result or in an inverse analysis for the identification problem. Finally, the conclusions drawn during the virtual testing of a monitoring system leads to an improvement of its performance and inspection capabilities.

Considering the inspection procedure of a structure, the task of simulation is to support an SHM system at as many levels as possible. Starting with the fundamental task of an SHM system, damage detection, some demands on the simulation method for wave propagation may be proposed. The crucial aspect of the simulation of the SHM, as well as NDE/NDT, systems is the modeling of wave interaction with damage.

Depending on the material of a structural component, different damage types are considered. A reliable damage model is key to the success of the simulation method for SHM. The wave interaction with damage may be thought of as an interaction with an interface of two media of high impedance mismatch. This requires special boundary conditions and a very accurate modeling approach, otherwise the structure's response to damage will be of no use and the modeling method discredited. The possibility to simulate such complex phenomena and the wave interaction with damage allow for full exploitation of the monitoring system's potential.

3.1.1 Wave Propagation in Piles and Soil

Sonic waves are very common in the subsurface. The cause can be natural, like earthquakes, or they can be man-made, like vibrations from trains, machinery, traffic, or purposely introduced with a hammer. In this section the basics of wave propagation in piles and soil is explained. The properties of the waves depend on the type of source and the medium through which the wave propagates. For example, a hammer impulse will create very high frequency vibrations when compared to an earthquake. The medium of the wave dictates the amplitude of the vibrations and how fast and far the waves propagate. First waves in a homogeneous medium are discussed. This is followed by wave propagation in non-homogeneous media and the phenomena that arise when waves pass through piles and layered soils.

3.1.2 Propagation Through Homogeneous Materials

When a pile is impacted with a single small temporary load, elastic strains travel through the material like a wave. These vibrations are both lateral and longitudinal, created by two main types of body waves:

1- Longitudinal vibration, parallel to direction of wave propagation, is created by p(pressure)-waves.
2- Lateral vibration is perpendicular to propagation direction and created by s(shear)-waves. If a medium cannot carry shear loads, the s-wave is not transmitted.

Another distinction can be made between compressional waves and tensional waves. Compression waves causes local shortening of the vibrating medium while tensional waves cause lengthening.

3.1.3 Propagation in a 1D Pile

In practice piles are mostly loaded in compression, so compression waves are created. At the end of the pile the wave is partially reflected. If the end is free, a tensional wave is reflected. If the end is not free, like when the pile is embedded in hard rock, the reflected wave will be compressional. The top of the pile is often free so the second reflection is mostly the opposite of the first reflected wave.

3.1.4 The Wave Propagation Equation

When modeling the propagation, the 1D wave equation is often used, as follows:

$$\frac{\delta^2 w}{\delta z^2} = c^2 \frac{\delta^2 w}{\delta t^2} \tag{3.1}$$

The local displacement of the medium (*w*) depends on the wave speed (*c*), time (*t*), and a spatial variable (*z*).

3.1.5 Determining Wave Velocity

The speed of the wave is based on material properties and varies for each type of wave. Equations 3.2 and 3.3 show the theoretical values for p-wave speed (cp) and s-wave speed (cs) respectively where ν [−] is the Poisson's ratio, E [kPa] is the Young's modulus, and ρ[kN.m−3] is the density [Liao et al., 2005]. P-waves are faster than s-waves.

$$\mathcal{C}_{\mathcal{P}} = \sqrt{\frac{(1-\mathcal{V})\,E}{(1-\mathcal{V})\,(1-2\mathcal{V})\,\rho}} \qquad ms^{-1} \tag{3.2}$$

$$\mathcal{C}_{s} = \sqrt{\frac{E}{\rho}} \quad ms^{-1} \tag{3.3}$$

The values in equations 3.2 and 3.3 are not always available, which means that other correlations are needed. A way of in-situ investigations is done using the Cone Penetration Test (CPT). Empirical correlation between shear wave speeds and CPT results have been found from numerous field tests in combination with seismic testing. These are often very site specific and contain large error margins. It is also possible to determine wave speeds using seismic CPT's (SCPT) in which vibrations from hammer blows are measured in sensors placed in the cone. This test will produce a series of vibrations at varying depths. The arrival time (a.t) of the wave is compared to the arrival 50 cm higher or lower to determine the time needed for the wave to propagate through those 50 cm. This will lead to the local wave speed.

3.1.6 Propagation Through Non-Homogeneous Material

Propagation through layers of varying material properties is more complicated. When a wave travels into another medium, multiple phenomena might occur.

a- Reflection in a pile: When a wave travels from one medium into another, it partially reflects. This is due to a change in impedance (Z), defined in equation 3.4 for piles. Here A is the area of the cross section. Z changes if the material or the shape or size of the cross-section changes. Therefore, defected or weakened concrete causes reflections.

$$\mathcal{Z} = \frac{E\,A}{c_s} \tag{3.4}$$

If a homogeneous pile is constructed in layered soil, reflections will still occur. Changes in soil stiffness affect the impedance of the pile locally, such that reflections are caused at the depths of changing soil. In addition, at the boundary of the pile, waves are also reflected. The nature of the reflection depends on whether impedance increases or decreases and by how much.

b- Reflection in soil: When waves pass through multiple layers of soil, reflections also occur. Again, this is caused by a change in impedance. Equation 3.5 gives the impedance of soil, where M is the stiffness modulus of the soil. This impedance is based on soil that is expected to be confined perpendicularly to propagation direction.

$$\mathcal{Z} = \frac{\mathcal{M}}{c_s} \tag{3.5}$$

c- Transmission: Besides reflection, when a wave travels from one medium to another, some of the vibrations are also transmitted. Due to the change in material, the wave will change speed. Transmission occurs when waves reach the boundary of the pile and energy is transmitted into the surrounding soil. Since the speed changes, if it arrives at an angle towards the normal of the boundary (known as the incidence angle), the direction of the wave changes as well. This occurs according to Snell's law illustrated in Figure 3.1 and Equation 3.6. The law applies to both p-waves and s-waves.

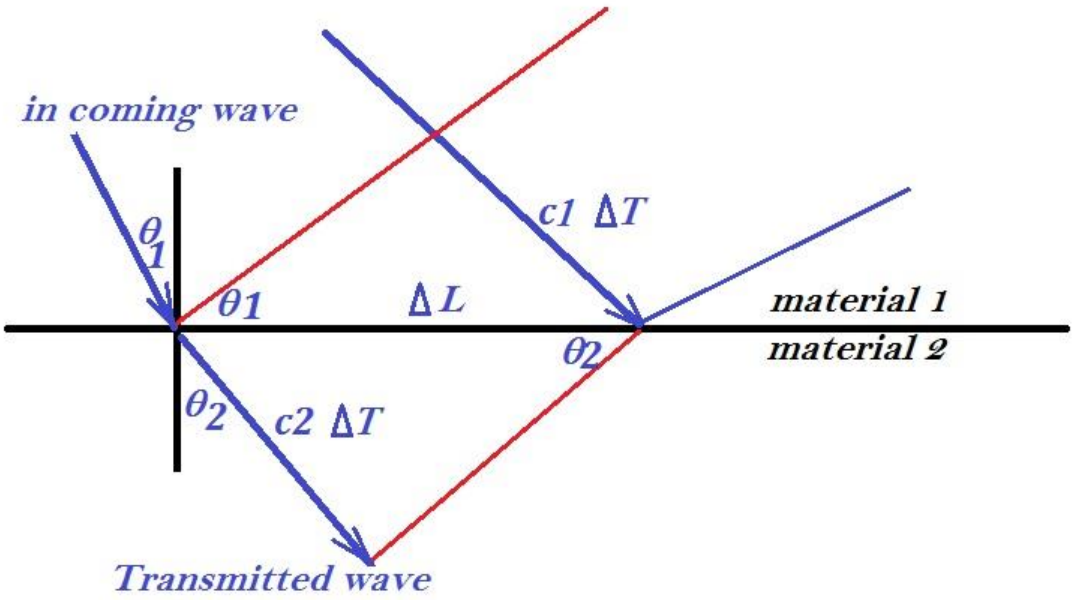

Figure (3.1): Incoming Wave Transmitted Due to Change in Medium.

$$\frac{\Delta T}{\Delta L} = \frac{\sin\theta_1}{c_1} = \frac{\sin\theta_2}{c_2} \qquad \textit{(Snell's law) (3.6)}$$

Both angles $\theta 1$ and $\theta 2$ give the orientation between the direction of wave propagation and the material boundary. ΔT is the time it takes for either wave to travel an arbitrary distance $\Delta L \sin(\theta 1)$. $\theta 1$ and $\theta 2$ are limited between 0 and $\pi/2$. This means that when $c2 > c1$ and $\theta 1$ is above a certain critical value, $\theta 2$ is limited to $\pi/2$. In this case the wave will propagate along the surface of the boundary, creating surface waves.

d- Surface waves: When a wave propagates along a boundary surface, surface waves arise. The surface could be the top of the pile or a boundary between two different soil types. These waves contain both longitudinal and transversal deformations and by definition the amplitude decreases further away from the surface.

e- Reflection at an angle: When a wave comes across a boundary at an angle ($\theta 1 \neq 0$), it will be reflected at an angle. The reflected wave has the same incidence angle as the incoming wave since they have the same wave speed. There is however an extra phenomenon which occurs in this situation. When the equilibrium of stresses is studied, it becomes clear that a second wave needs to be generated at the boundary. Figure 3.2 shows the direction of stresses of an example. If the incoming wave at a horizontal boundary is a p-wave, a p-wave is reflected. But to maintain horizontal equilibrium, an s-wave is generated. In addition, since s-waves travel at another velocity, it is reflected at another angle which can be found according to Snell's law in equation 3.6. If the incoming wave is an s-wave, a p-wave and s-wave are reflected. In this case however s-waves are slower than p-waves, which might lead to the formation of surface waves when the incoming wave has an

incidence angle higher than the critical angle mentioned above. With the same reasoning, during transmission, a second wave type is formed as well.

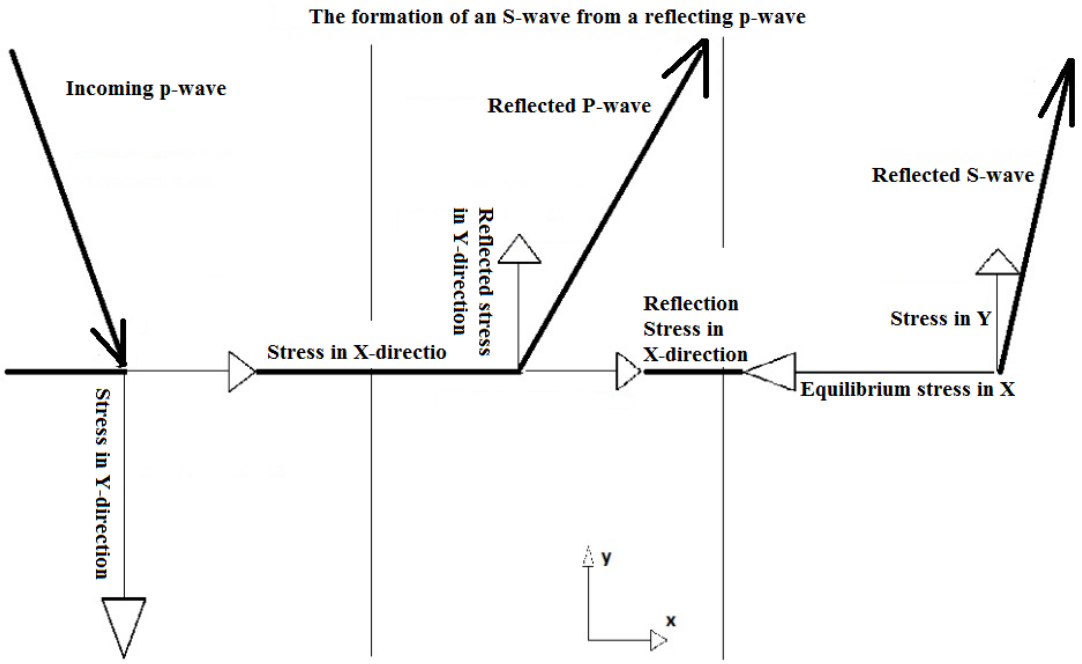

Figure (3.2): Incoming Wave Reflected Due to Change in Medium.

3.2 Software Used in Analysis "ADINA"

The finite element method (FEM) is a method for solving differential equations by utilization of 'subdomains', called elements, in which it is assumed that the solution type is known. Then a structure is discretized by using elements, composing a mesh, which represents the investigated domain. Although the most intense development of the method is credited to the 1960s and later, the first ideas of FEM date back to the nineteenth century. The first concept of substitution of a general solution to a continuum body by a set of primitive geometrical shapes with assumed solution types was proposed by Kirsch (1868) [xx]. There are a few formulations of FEM. The two main groups of approaches are based on:

(a) Variational method; and (b) Weighted residuals methods. Both provide a means for the solution of mechanical systems. The variational method makes use of a functional, a kind of integral formulation, that may be used, by invoking the stationary condition, for finding equilibrium. In the case of mechanical systems, the mechanical energy of a system may be the functional. Then, the stationary condition corresponds to the minimum of mechanical energy. Therefore, it is possible, knowing only the mechanical energy of a system, to find the equilibrium configuration.

This provides a versatile and general tool for analyzing mechanical systems. The methods of weighted residuals operate directly on differential formulations for a given problem. Substituting any function that is not the true solution to the differential equation produces an error, called a residual. In such a case, changing the trial solution and evaluating the residual enables finding the closest possible solution to the differential equation. Of course, the smallest possible residual (equal to zero in the limit), provides the best solution. Moreover, the residual is weighted and the product is integrated, to improve the solution process and to impose additional constraints within the domain.

3.2.1 Three-Dimensional Solid Elements

a- General Considerations

The three-dimensional (3-D) solid element used is 8 nodes elastic isoperimetric element applicable to general 3-D analysis as shown

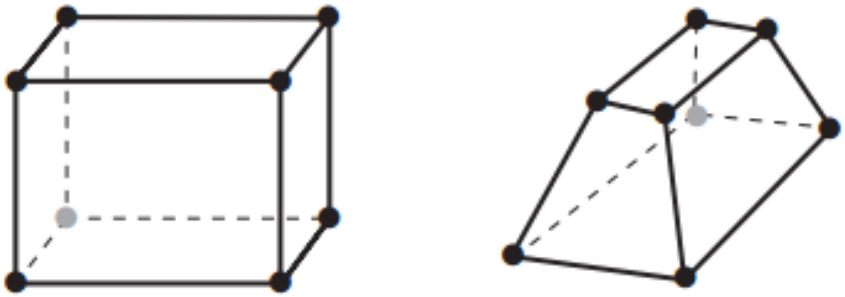

Figure (3.3): Three-D 8 Nodes Finite Element Employed in the Model.

The 3-D solid element should be employed in analyses in which the three-dimensional state of stress (or strain) is required or in which special stress/strain conditions, as for two-dimensional solid elements do not exist. The elements usually used are iso-parametric displacement-based finite elements. The basic finite element assumptions for the coordinates.

$$\mathcal{X} = \sum_{i=1}^{q} \hbar_i \; x_i \qquad \mathcal{Y} = \sum_{i=1}^{q} \hbar_i \; x_i \qquad \mathcal{Z} = \sum_{i=1}^{q} \hbar_i \; x_i \qquad (3.7)$$

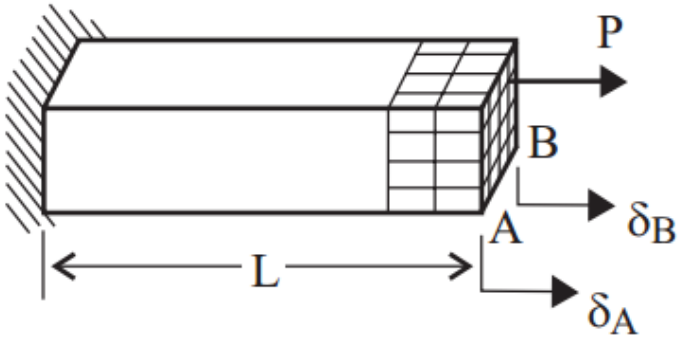

Figure (3.4): Plane Sections Do Not Remain Plane $\delta_A \neq \delta_A$

The basic finite element assumptions for the coordinates for the displacements:

$$\mathcal{U} = \sum_{i=1}^{q} \hbar_i \; u_i \qquad \mathcal{V} = \sum_{i=1}^{q} \hbar_i \; vx_i \qquad \mathcal{W} = \sum_{i=1}^{q} \hbar_i \; xw_i \tag{3.8}$$

where;

hi (r, s, t) = interpolation function corresponding to node i.

r, s, t = isoperimetric coordinates.

q = number of element nodes, which is 8.

xi, yi, zi = nodal point coordinates.

ui, vi, wi = nodal point displacements.

The 3-D elements can be used with a small displacement/small strain. The use of a linear material with the small displacement/ small strain formulation corresponds to a linear formulation

b- Numerical Integration

For the calculation of element matrices to hexahedral (brick) elements 8 nodes, Gauss numerical integration is used. The default Gauss integration orders are 2×2×2 for the 8-node. in geometrically nonlinear analysis, the spatial positions of the Gauss integration points change continuously as the element undergoes deformations, but throughout the response the same material particles are at the integration points. The convention for the integration point numbering used in the stress output is as follows: The first integration point is the point with the most negative location in r, s and t. The next integration points are located by increasing t (and label INT) successively up to its maximum positive value, then increasing s (and label INS) one position towards positive and varying t again from its maximum negative to its maximum positive values, and so on as shown in Figure 3.5.

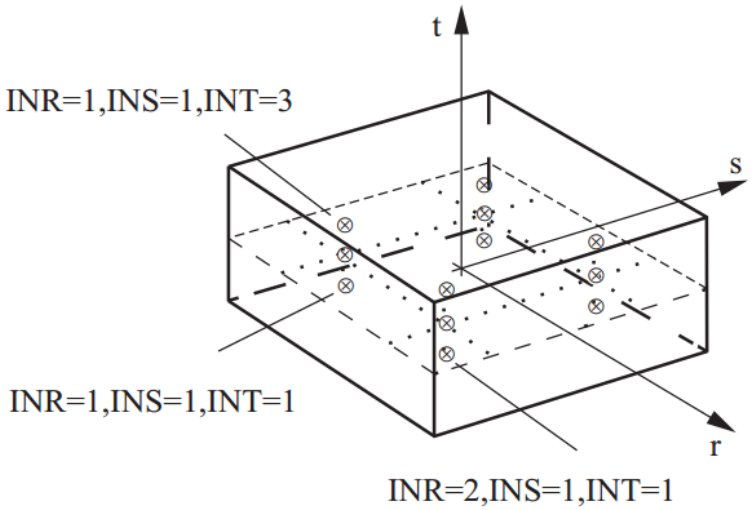

Figure (3.5): Integration order in r-s plane=2, Integration order in t-direction=3

c- Mass Matrices

The consistent mass matrix is always calculated using 3×3×3 Gauss integration. The lumped mass matrix of an element is formed by dividing the element's mass M equally among each of its n nodal points. Hence the mass assigned to each node is M / n. No special distributory concepts are employed to account for element distortion.

d- Gauss Integration

The lumped mass matrix of an element is formed by dividing the element's mass M equally among each of its n nodal points. Hence the mass assigned to each node is M / n. No special distributary concepts are employed to distinguish between corner and mid-side nodes, or to account for element distortion. n is the number of distinct non-repeated nodes in the element. Hence, when an element side or face is collapsed to a single node, the total mass of the element is divided among the unique nodes in the element.

e- Stresses

Each element outputs the following information to the porthole file, based on the material model. This information is accessible in the AUI using the given variable names. In ADINA, the stresses are calculated using the strains at the point of interest. The stresses are not smoothed. The AUI can be employed to calculate smoothed stresses from the results output by ADINA. Stress measures: The stress measures used in ADINA of a rod under uniaxial tension.

Stress Equation $\sigma = \frac{\mathcal{F}}{\mathcal{A}_o}$ (3.9)

f- Locations Where Results Are Saved

The results are saved either at the element integration points or at the element corner nodes. When the results are saved at the integration points, the stresses are calculated using the strains at the point of interest. The AUI can be employed to calculate smoothed stresses from the results output by ADINA. When the results are saved at the element corner nodes, the number of points per element at which results are saved is significantly reduced.

g- Nodal Forces

The nodal forces that correspond to the element stresses can also be requested in ADINA. This force vector is calculated in a linear analysis using

$$\mathcal{F} = \int_{\mathcal{V}} \mathcal{B}^{\mathcal{T}} \tau \, d_{\mathcal{V}} \quad (3.10)$$

where B is the element strain-displacement matrix and τ is the stress vector. The integration is performed over the volume of the element.
The 8-node brick element should only be used in analyses when bending effects are not significant.

3.2.2 Stress and Strain Measures in ADINA

It is important to decide which stress and strain measures are employed in the use of our material model. In the preparation of the input data in which the material parameters are defined with respect to these stress and strain measures. In the interpretation of the analysis results in which the type of stresses and strains output must be considered. The practical use of the material models available in ADINA. Regarding the stress and strain measures used for the input data and analysis results is as follows: -

In the following discussion, small strains are strains less than about 2%.

Small displacement/small strain formulation

Input of material parameters: All elements and material models use the engineering stress-engineering strain relationship.
Output: All elements and material models output engineering stresses and engineering strains.

Strain measures:

The strain measures used in ADINA are illustrated hereafter in the simplified case of a rod under uniaxial tension.

Engineering strain $e_o = \frac{\ell - \ell_o}{\ell_o}$ (3.11)

In the small strain formulations, the current area is always assumed to be equal to the initial undeformed area. Engineering strains are also called nominal strains

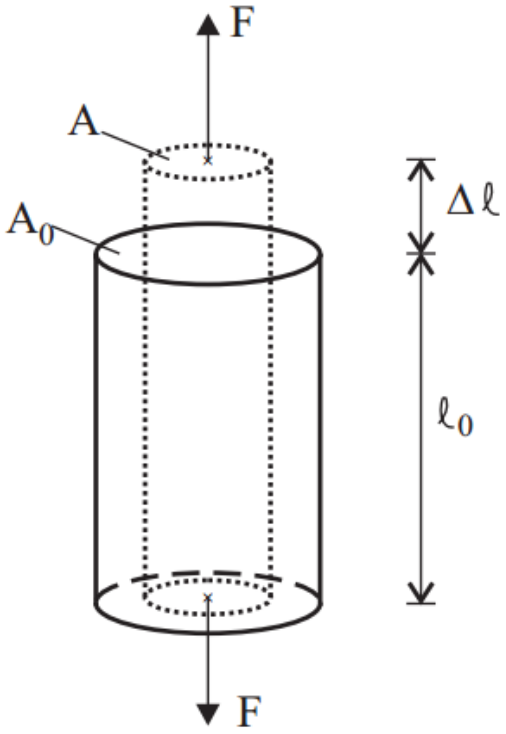

Figure (3.6): Cross section Ao, A, Force F, Initial Length l, Strain lo

where A_o is the initial section area, A is the final section area, F is the applied force and l equals $l_o + \Delta l$

3.2.3 Linear Elastic Material Model

Elastic-isotropic material model

At the isotropic linear elastic model, the total stress is uniquely determined by the total strain. These models can be employed using the small displacement or large displacement formulations. In all cases, the strains are assumed small. When the elastic-isotropic and elastic-orthotropic materials are used with the small displacement formulation, the formulation is linear.

This material model is available for the 3-D elements. In the small displacement formulation, the stress-strain relationship is

$$ {}^{t}_{0}\sigma = \mathcal{C}\ {}^{t}_{0}e \qquad (3.12) $$

In which ${}^{t}_{0}\sigma$ is the stress

and ${}^{t}_{0}e$ is the strain

The two material constants used to define the constitutive relation (The matrix C) are :

E = Young's modulus, v = Poisson's ratio

The same constants are employed in the small and large displacement formulations, and hence the matrices [C] are identically the same in all formulations. The model used eight nodes model The soil is modeled in Mohr-Columb material with angle of friction 30° and density 19.0 kN/m^3. The foundation is concrete with 2.25e4 MPa elasticity modulus and 25.0 kN/m^3 and 0.2 Poisson's ratio.

3.2.4 Stress Integration Procedure

If the stress calculation at t + Δt is solely based on the state at t +Δt,

$$ {}^{t+\Delta t}\sigma = f\ (\ {}^{t+\Delta t}e\ ,\ {}^{t+\Delta t}T\ ,\ldots\ ) \qquad (3.13) $$

then it is the most straightforward to implement, and includes elastic and hyper-elastic materials. However, for incremental or rate type functions, or such as

$$ \dot{\sigma} = f\ (\ \dot{e}\ ) \qquad (3.14) $$

The user must decide between single and multi-step calculation and also between implicit or explicit stress calculation.

Sub-Incrementation

Sub-incrementation can be used for forward stress integration. In this case, instead of going from time t to time t + Δt in one step, sub-increments are used. Sub-increments can be forward in time from time t to t + Δt in k steps as shown in Figure when Δτ = Δt/k. The time forward sub-incrementation can be used with both implicit or explicit stress integration.

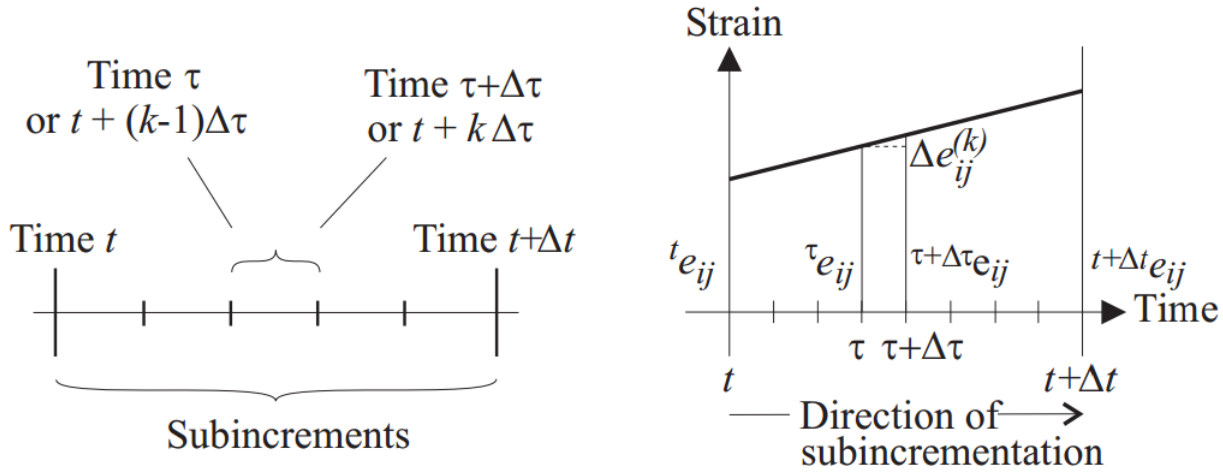

Figure (3.7): Schematic of forward time incrementation

3.2.5 Three Dimensional Solid Elements

• The user-supplied algorithm for the user-coded material model for 3-D solid elements must be placed in subroutine UCMAT3(appendix).
• The convention used for stresses and strains is shown in Figure (3.7).

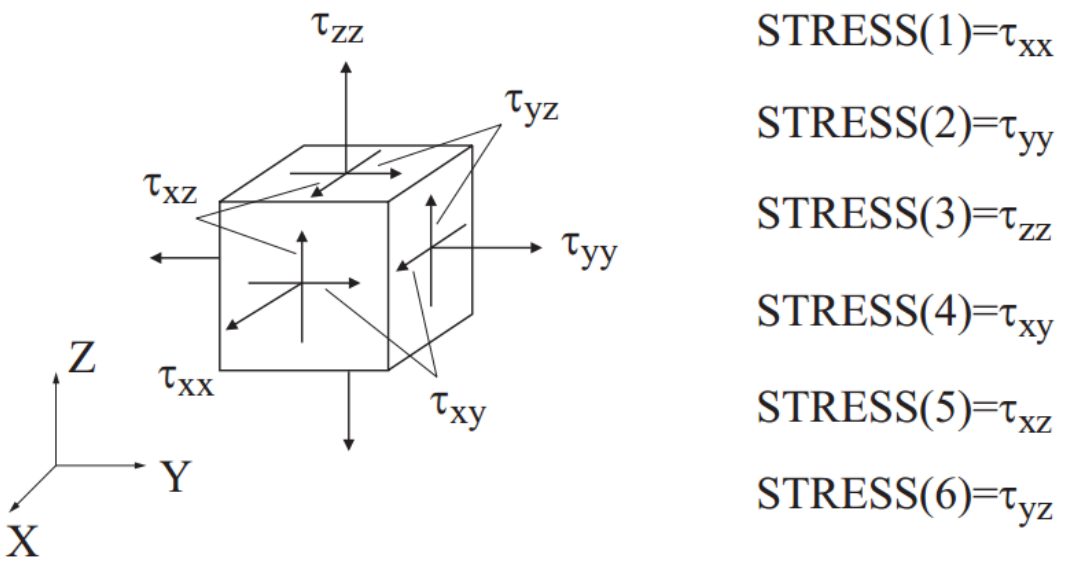

Figure (3.8): Stress/ strain convention for 3-D elements.

3.2.6 Linear Dynamic Analysis.

The following procedure is the used one in ADINA for solution of the finite element equations in a linear dynamic analysis:

Step-by-step direct integration through implicit time integration using the Newmark method

• The governing equilibrium equation at time t+Δt is given by

$$M\ {}^{t+\Delta t}\ddot{U} + C\ {}^{t+\Delta t}\dot{U} + K\ {}^{t+\Delta t}U = {}^{t+\Delta t}R \qquad (3.15)$$

$$where\ ,$$

$$\mathrm{M} = \text{constant mass matrix}$$

$$\mathrm{C} = \text{constant damping matrix}$$

$$\mathrm{K} = \text{constant stiffness matrix}$$

$${}^{t}R\ ,{}^{t+\Delta t}R = external\ load\ vector\ applied\ at\ time\ t, t+\Delta t$$

$${}^{t}\dot{U}\ ,{}^{t+\Delta t}\dot{U} = vectors\ of\ nodal\ point\ velocities\ at\ time\ t, t+\Delta t$$

$${}^{t}\ddot{U}\ ,{}^{t+\Delta t}\ddot{U} = vectors\ of\ nodal\ point\ accelerations\ at\ time\ t, t+\Delta t$$

$$U = vector\ of\ nodal\ point\ displacement\ increments\ from\ time\ t\ to\ time\ t+\Delta t$$

3.2.7 Choosing between Implicit and Explicit Formulations

The main criterion governing the selection of the implicit or explicit formulations are the time scale of the solution. The implicit method is used in this analysis because it provides higher accuracy, unconditionally stable, along with allowing for larger time step size.

Chapter Four

Results and Discussion

Chapter Four

Results and Discussion

4.1 Pile Model

There are many shapes of defects in concrete piles such as; cracking, honey-combing, bulges, and necking. Necking is a reduction in cross sectional area of the pile, while bulges are increases in the pile cross sectional area. The integral (healthy) pile is that one having constant diameter along its whole length with no cracks, necking, bulges, or honey-combing. Non-destructive tests with dynamic loads are used to predict the location of pile defects. One of the most familiar tests used for this target is the pile integrity test (PIT), which is fast, common, and low-cost test. The mechanism of (PIT) is that the wave transfer from pile head to pile toe then return to the top. Although, the (PIT) is a fast and reliable test, there are some shortcomings of this test.

4.1.2 Modeling

Studied concrete piles are considered to have circular cross-sectional area and totally embedded in the soil. The pile radius varied from 40 to 120 cm, with all having the same length of 12 meters. An axisymmetric model is used in modeling the pile and the surrounding soils, with soil domain radius equal to 24 m plus the pile diameter, and a height of 24 m. The same meshing pattern is used in all the models having the same incremental values, sequence, and order, thus, avoiding the effect of meshing on the results. Table (1) presents the properties of the soil and the pile materials used in the numerical analysis.

Table 4.1: Properties of the Studied Soil and Concrete Materials.

Materials	Numerical model	Young's Modulus (MN/m^2)	Density (kN/m^3)	Poisson's Ratio	Friction Angle (degrees)
Concrete	Elastic isotropic	2.1×10^3	25.0	0.2	N/A
Soil	Mohr-Coulomb	1.0×10^2	19.0	0.3	40

A very small value of Rayleigh damping stiffness factor β for the pile is assumed = 70×10^{-7}, while Rayleigh damping mass factor α for the pile is assumed to be zero. In addition, Rayleigh damping stiffness factor β and mass factor α for the soil is considered = zero. These very small values are mainly chosen due to the very short duration of monitoring the incident wave, so that it's considered that the damping effect will not affect the behavior before a relatively long duration. The dynamic load used in this research is an impact load. It modeled in ADINA software as concentrated load equal to 2.5 N applied at the pile head, with time function as presented in Figure (1). The considered solution steps are 50 steps during the pulse duration which equals 0.001 sec, then 400 steps from 0.001 sec to 0.017 sec. For solving the finite element equations in a linear dynamic analysis, ADINA employed the step-by-step direct integration through implicit time integration using the Newmark's method.

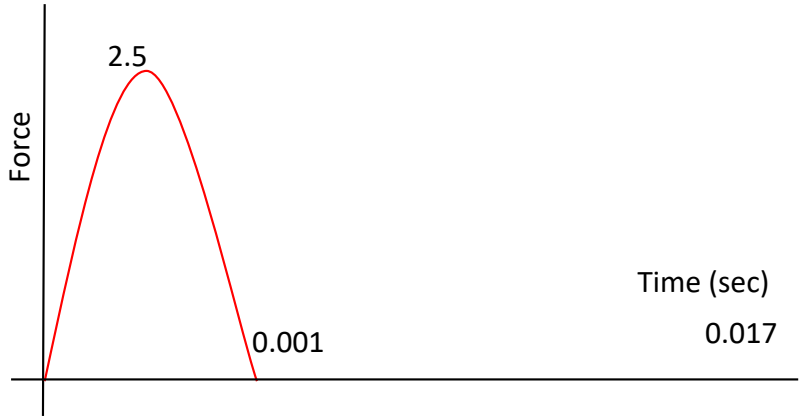

Figure (4.1): Force Time Function of Dynamic Load.

The model increases laterally every 60 cm to respect the condition (mesh side should have a maximum length = $C \times t_c/2.5$. The wave velocity (C) = $\sqrt{E/\rho}$, where E is the concrete Young's modulus and ρ is the concrete density. Therefore, the wave velocity is taken equal to 3000 m/s. The time of impact load is 0.001 sec of a half sinusoidal wave and frequency 0.5 kHz. Lateral and cross-sectional meshes have the same dimensions at the necking zone. The element size within the mesh surrounding the pile is equal to 5 cm in both directions. 3D-model of the pile and the surrounding soil is shown in Figure (4.2).

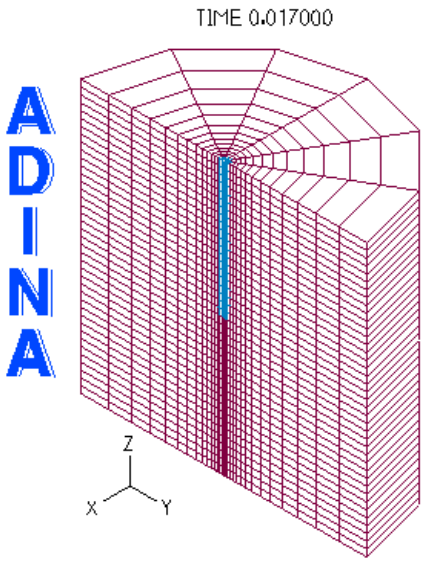

Figure (4.2): Finite Element Axisymmetric Model for the Intact Pile Case.

Regarding the boundary conditions, the bottom boundary is fixed with no movements in X, Y, and Z directions. However, the side boundaries are rollers in the vertical directions to allow for soil settlement, as shown in Figure (4.3). Larger mesh sizes are used in the analysis to assess the effect of mesh size convergence. The chosen mesh size along with the FEM discretization showed no difference in the results between the used mesh and the smaller ones indicating the accuracy of the used mesh. This may be attributed to the relatively short time of solution which is 0.017 sec also the relatively low applied point load value which is 2.5 N to the model mass.

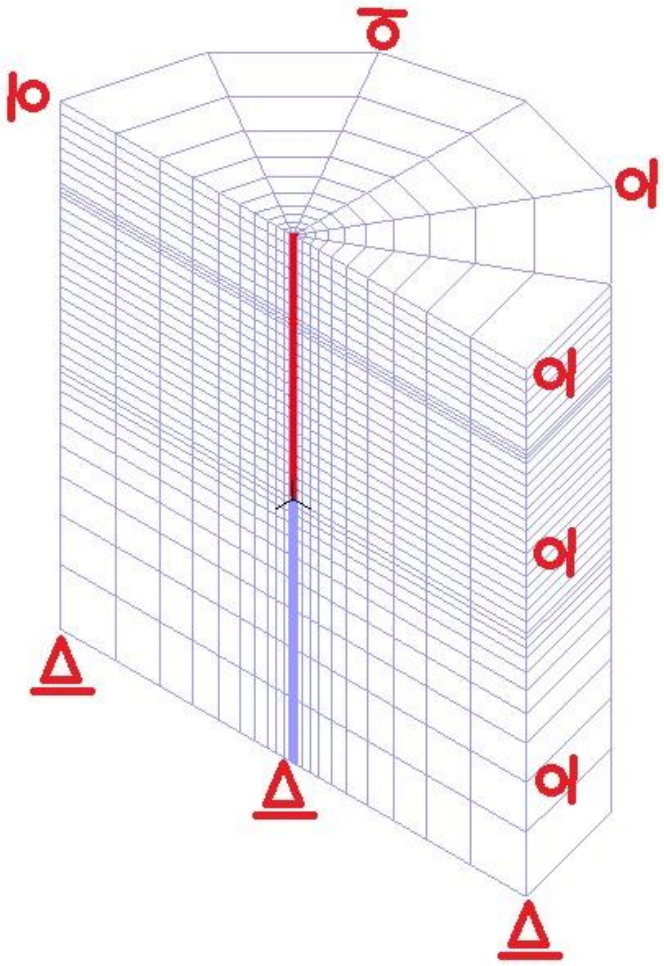

Figure (4.3): Boundary conditions of the Finite Element.

4.1.3 Studied Cases

A parametric study is performed in which the following parameters are studied in details: Pile diameter varying from 40, 60, 80, 100 and 120 cm. Notch or necking in three different locations, upper, middle third, and lower third. Four notch or necking sizes, as reduced from the pile diameter, having sizes of 12.50%, 25.0%, 37.5%, and 50.0% are deducted as notch from the pile diameter.

4.1.4 Results of the Analysis

Relationship between time and velocity at a specific point are studied for all cases. The location of the studied point is at (1/3 * pile radius) from the pile center. Different parameters are studied including; pile diameter, necking diameter, and the ratio between them. Obtained curves are compared with the PIT manual schematic diagram. Figure (4.4) shows the velocity time history at the studied point located on the surface of intact pile with diameter = 100 cm. It is found that there are two marked parabolas (a and z). Parabola (a) is the pulse induction and named as the initial parabola. Initial parabola is induced directly due to the impulse effect not as the same parabolas along the response history which induced after the pulse release. Initial parabola is found as smooth peak in smaller diameters 40 cm and 60 cm and gradually noised from 60 cm then 80 cm then 100 cm then 120 cm. This declares the direct relation between the pulse frequency effect on the PIT test and gives an obvious observation that for every pile diameter there is an optimum frequency. Parabola (z) is the terminal parabola or the end parabola, and it means that the wave has reached the pile end and reflect. The symbol t_{lp} in Figure (4.4) expresses the time indicating the distance between the pile head and its end bearing point along the whole pile length. The end parabola will show a conclusion as its trend is affected by necking and

also its shape changes with noisy waves in the initial parabolas. In addition, it should be noted that the responses don't drop down to less than zero from time $2*10^{-3}$ sec to time $8*10^{-3}$ sec.

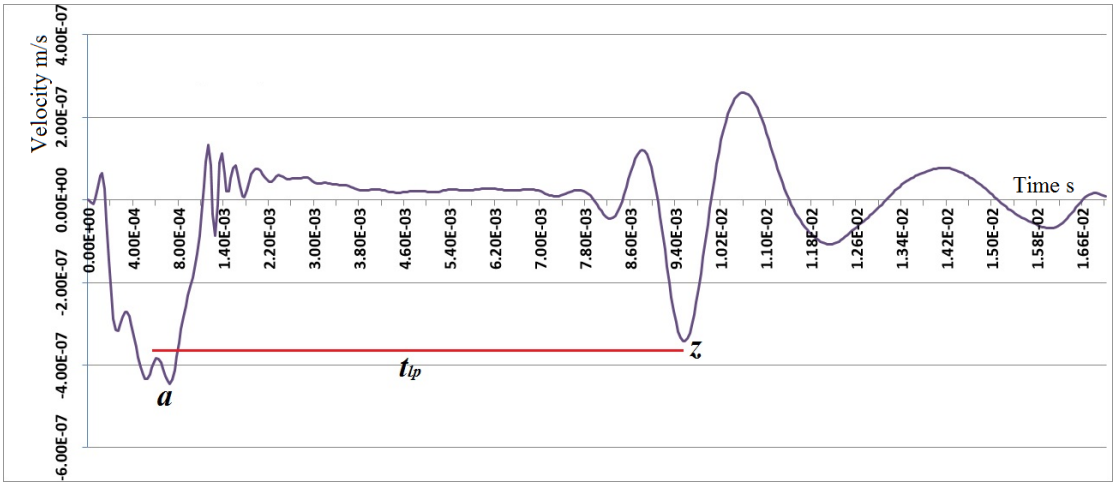

Figure (4.4): Velocity Response for an Intact Pile of 100 cm Diameter.

Figure (4.5) presents a comparison of velocity time history between intact pile with D = 100 cm and four different necking values. All four necked piles have a necking at the upper third zone of the pile length. The necked pile diameters are 87.5, 75.0, 62.5 and 50.0 cm, with diameter reduction of 12.5, 25.0, 37.5, and 50.0 cm respectively. The symbol t_{lu} in Figure (4.5) expresses the time indicating the distances between the pile head and the necking location. The symbol t_{lp} in Figure (4.5) expresses the time indicating the distance between the pile head and its end bearing point along the whole pile length. It is noticed that the part [Q] of the graph increases downward when the pile diameter decreases, or when the necking increases.

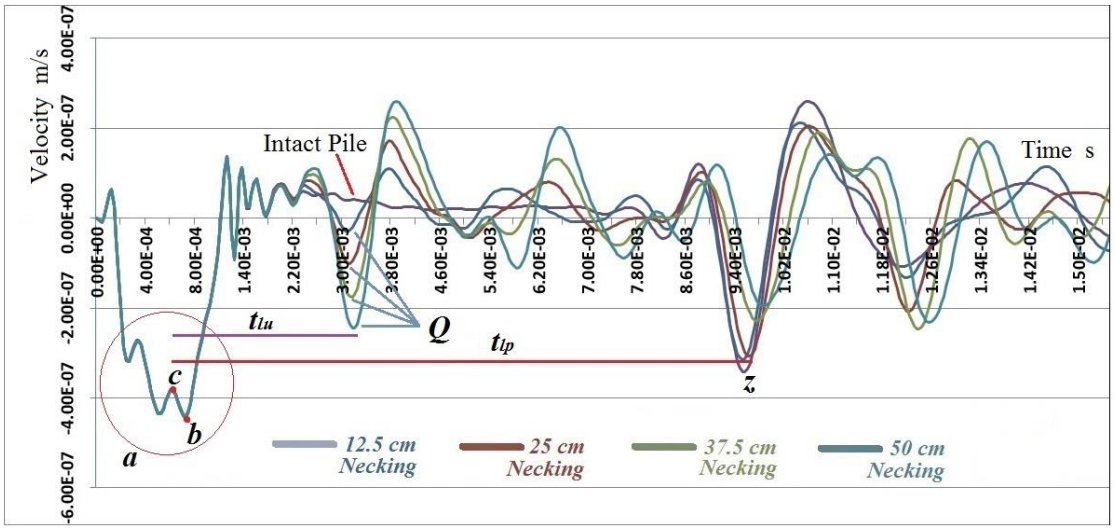

Figure (4.5): Velocity Response for an Intact Pile 100 cm Diameter versus Four Defected Piles at Upper Third of the Pile Length.

where

Q : is the negative peak velocity just after the initial zone, (m/sec.);

a : is the zone of noise that took place in the initial parabola;

b : is the lowest peak in the initial noise zone;

c : is a noise point just preceding the lowest peak in the initial noise zone.

Figure (4.6) presents a comparison of velocity time history between intact pile (D = 100 cm) and four necked piles. All four necked piles have a neck at the middle of the pile length. The necked pile diameters are 87.5, 75.0, 62.5 and 50.0 cm. The symbol t_{lm} in Figure (4.6) expresses the time indicating the distances between the pile head and the necking location. It is noticed that part [P] of the graph increases downward when the pile diameter decreases, or when the necking increases.

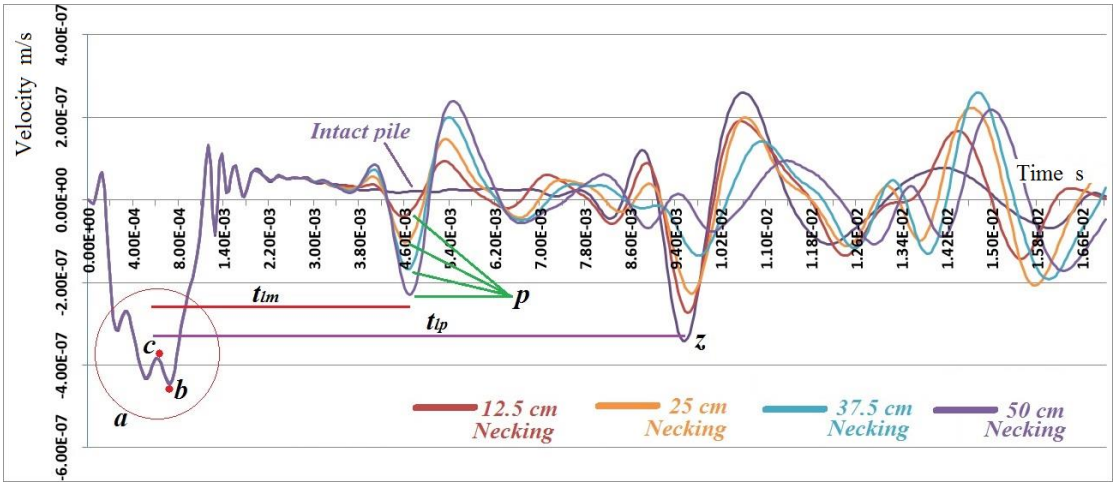

Figure (4.6): Velocity Response for an Intact Pile 100 cm Diameter Versus Four Defected Piles at the Middle of the Pile Length.

Figure (4.7) shows a comparison of velocity time history between the case of intact pile (D = 100 cm) and four necked piles with a neck at the lower third part of the pile length. The same necking ratios are used in this case also. The symbol t_{lb} in Figure (4.7) expresses the time that the wave travels over the first two thirds of the pile. It is noticed that the part [O] of the graph increases downward when the pile diameter decreases, or when the necking increases.

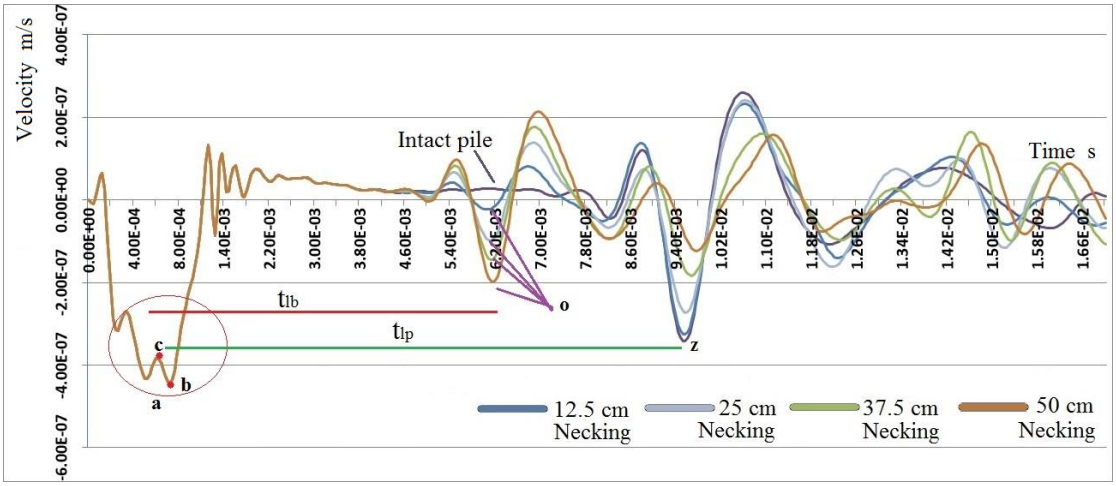

Figure (4.7): Velocity Response for an Intact Pile 100 cm Diameter Versus Four Defected Piles at the Lower Third of the Pile Length.

Figure (4.8) summarizes Figures (4.4), (4.5), and (4.6). It is noticed that there is a time shift on the velocity time history curves when the

location of the necking moves from the pile top to the pile middle or the pile bottom. The distance between the domain values is t_{lu}, t_{lm}, t_{lb} are proportional to the physical distances between the necking in the pile to the pile length expressed in the pile length domain value t_{lp}.

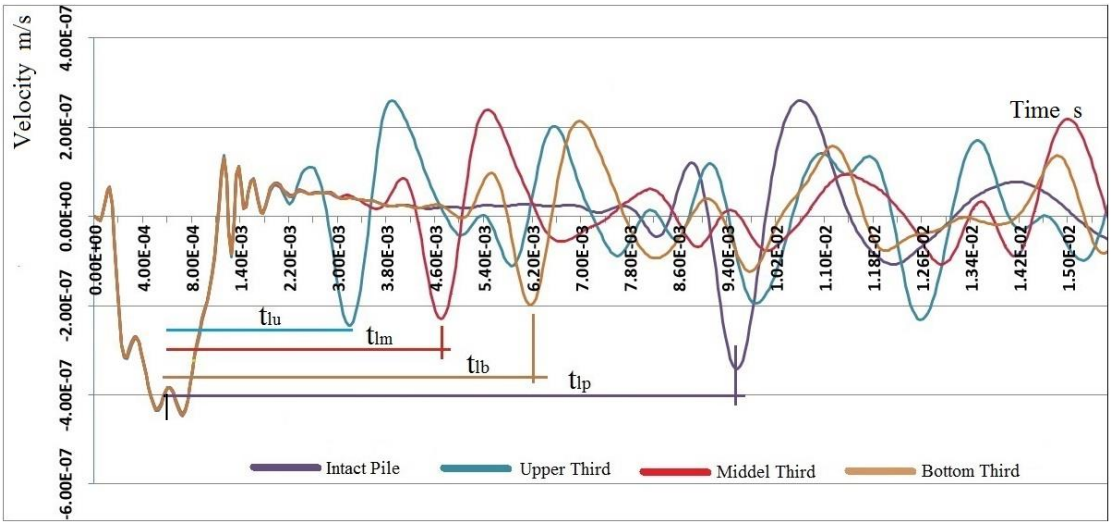

Figure (4.8): Velocity Response for an Intact Pile 100 cm Diameter Versus Three Defected Piles of 50 cm Necking at Upper, Middle and Lower Third of the Pile Length.

The behavior of the studied piles has a pattern which can be presented in Figure (4.10). It may be compared with the known PIT manual shape which passes through several operations of filtration and other mathematical computations to specify the defect location, as shown in Figure (4.9).

Pile profile	Description	Reflectogram
	straight pile ,free end ,length as expected	
	straight pile ,free end ,length as expected	
	Straight pile ,free end ,shorter thanexpected	
	Increased impedance	
	Decreased impedance	
	Locally increased impedance	
	Locally decreased impedance	
	High L/D ratio and/or high skin friction ,no reflection from pile toe	
	Multiple reflections from mid-length discontinuity - toe reflection indiscernible	
	Irregular profile - irregular reflectogram	

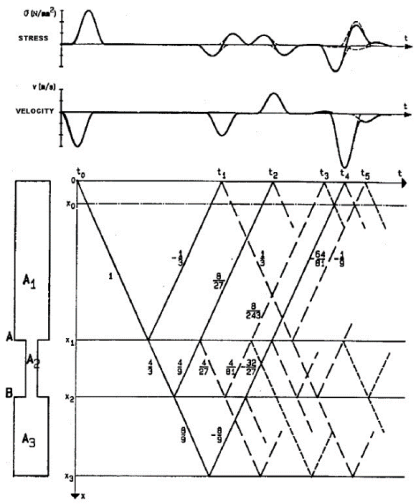

Figure (4.9): The PIT Schematic Diagram and Table. Amir, (2009).

The research schematic diagram has a new conclusion that it may introduce approximately the volume of the defect. In addition, it doesn't need any filtration, but just the directly introduced response and comparing the result with the new schematic diagram, as presented in Figure (4-10). On other hand, it can be said that the ratio between the notch diameter to the pile diameter is approximately equal to the ratio shown in the following equation; named as schematic diagram equation.

$$RD = \frac{y_1}{2 * y_2 - y_3} \qquad (4.1)$$

where:

y_1 : is the peak velocity of parabola [Q],

y_2 : is the velocity value at point [b],

y_3 : is the velocity value at point [c].

a, Q, b, and c are presented in Figures (4.5) and (4.10).

y_2 or (b) is the minimum value in the pulse parabola [a] and y_3 or (c) is the maximum y value in the pulse parabola [a]. It can be predicted whether the pile is intact or not using this formula. In addition, the location and the diameter of the necking can also be predicted.

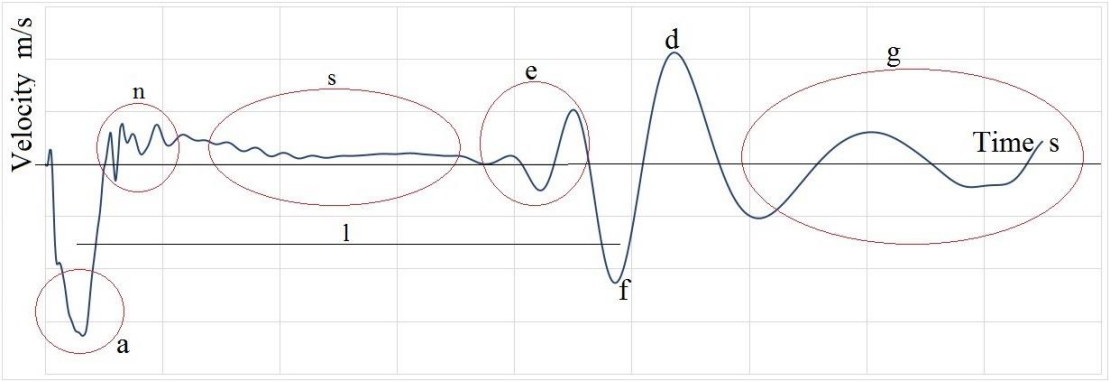

Figure (4.10): The Research Schematic Diagram.

Table 4.2: Schematic parameters definitions

a: Impact peak.	f: Minimum negative amplitude along the response whatever its duration.
s: Studied portion.	g: Noisy portion directly after maximum velocity response value.
d: Maximum positive amplitude along the response whatever its duration.	g: Noisy portion directly after maximum velocity response value.
n: Noisy portion directly after impact peak	e: Noisy portion directly beyond the minimum velocity response value.
L: Scoped response length	

4.1.5 Effect of Pile Diameter

The effect of pile diameter is shown in the following figures, knowing that the figures having similar trends of that of 100 cm pile diameter. Figure (4-11) presents a comparison of velocity time history between intact pile with D = 40 cm and four piles having different necking. All four necked piles have a neck at the upper third of the pile length. The necking (or reduction) in the pile diameter is 5, 10, 15 and 20 cm respectively. It is noticed that the part [Q] of the graph increases downward when the pile diameter decreases, or when the necking increases.

It is noticed that for pile diameters of 40 and 60 cm, shown in Figures (4.11) and (4.12), a separate single parabola with no inflection point appeared below the pile tip for the intact pile only in the negative zone. On the other hand, all piles with different necking zones are having one or more inflection points with much more distorted parabolas for larger necking zones. However, for pile diameters of 80, 100, and 120 cm, the peak of the parabola appeared in the positive zone just below the pile tip also. This may be attributed to that the frequency in the initial parabola induced a significant noise in larger diameters, as shown in Figures (4-5), (4-13), and (4-14).

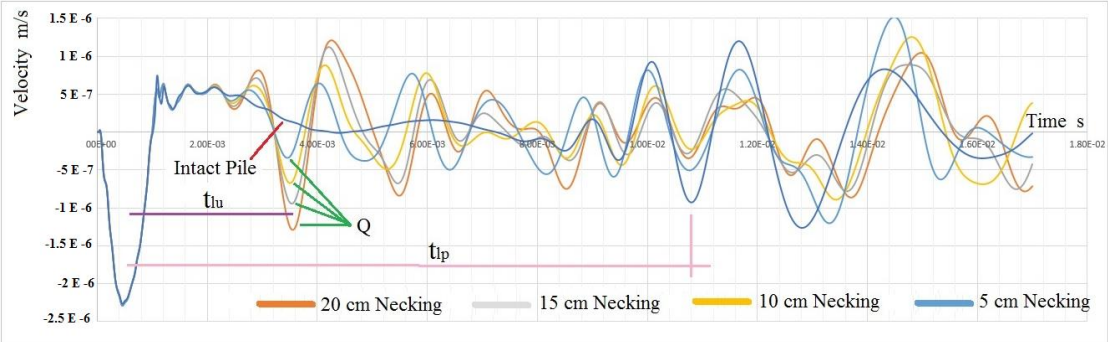

Figure (4.11): Velocity Response for an Intact Pile 40 cm Diameter Versus Four Defected Piles at the Higher Third of the Pile Length.

The same trend is noticed for different pile diameters, and shown in successive figures, Figure (4-12) for 60 cm diameter pile, Figure (4-13) for 80 cm diameter pile, and Figure (4-14) for 120 cm diameter pile.

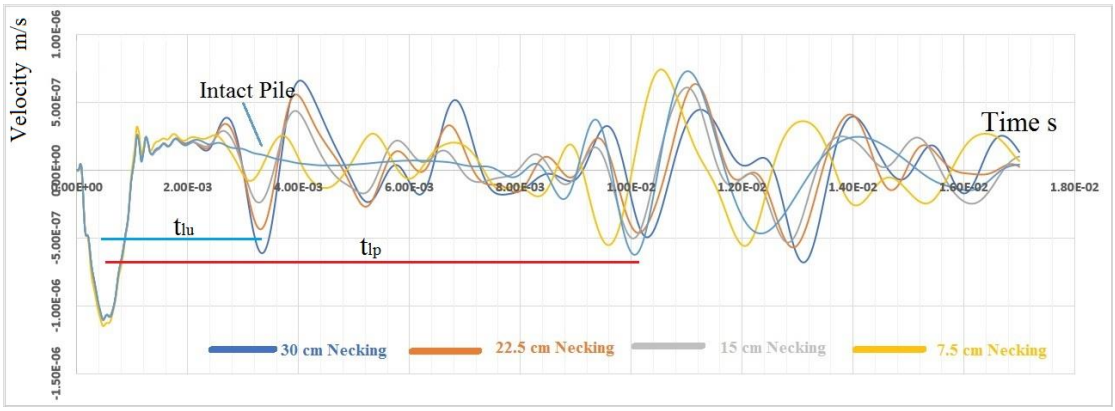

Figure (4.12): Velocity Response for an Intact Pile 60 cm Diameter Versus Four Defected Piles at the Upper Third of the Pile Length.

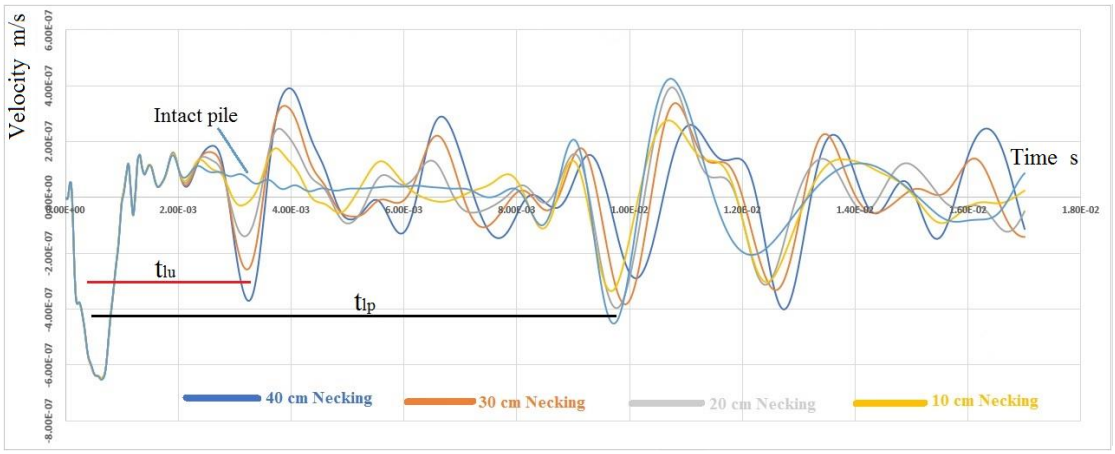

Figure (4.13): Velocity Response for an Intact Pile 80 cm Diameter Versus Four Defected Piles at the Upper Third of the Pile Length.

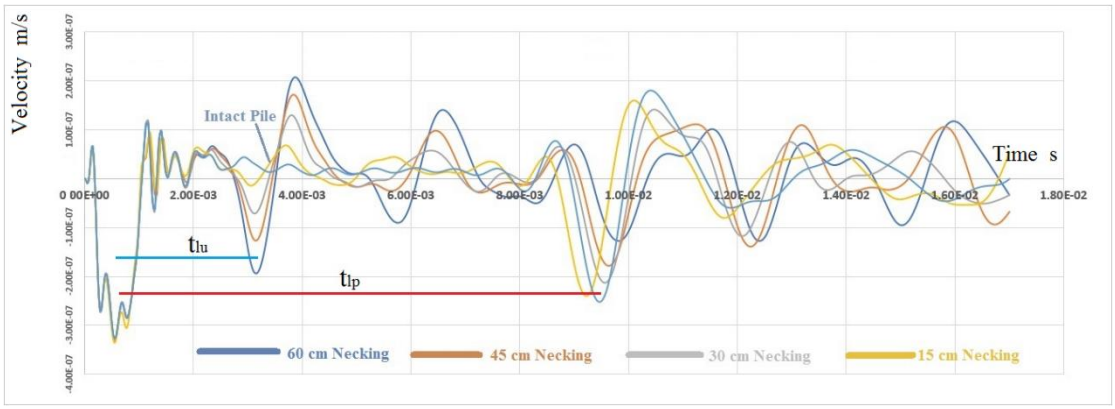

Figure (4.14): Velocity Response for an Intact Pile 120 cm Diameter Versus Four Defected Piles at the Upper Third of the Pile Length.

Figure (4.15) presents a comparison of velocity time history between intact piles with diameters D = 40, 60, 80, 100, and 120 cm. All

the five pile diameters have a common property, the response is always positive until it reaches the end of the pile, where reflection of the applied wave returns again. There is a relatively small shift between the end bottom parabola which may be due to noise that took place in the initial parabola.

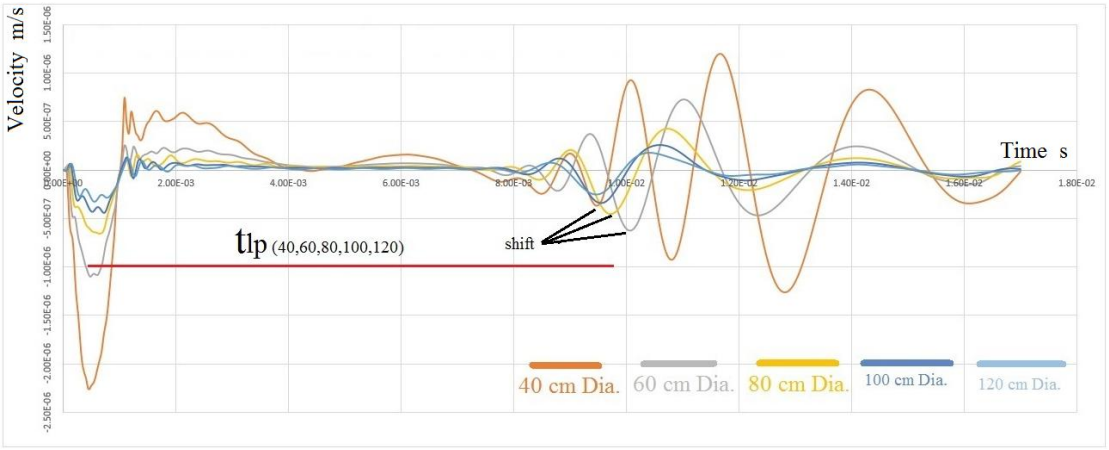

Figure (4.15): Velocity Response for Intact Piles of 40, 60, 80, 100, and 120 cm Diameter.

Figure (4.16) presents a comparison of velocity time history between piles with D = 40, 60, 80, 100, and 120 cm through initial parabolas only. As shown the figure, pile diameter of 40 cm has the deepest response and pile diameter of 120 cm has the shallowest. As the applied frequency is the same, the pile diameter effect is significant in the figure. The figure shows that frequency can be increased in piles of 100 and 120 cm diameters, which means results will be better, but its barely adjusted for piles of 40, 60 and may be present in pile diameter of 80 cm.

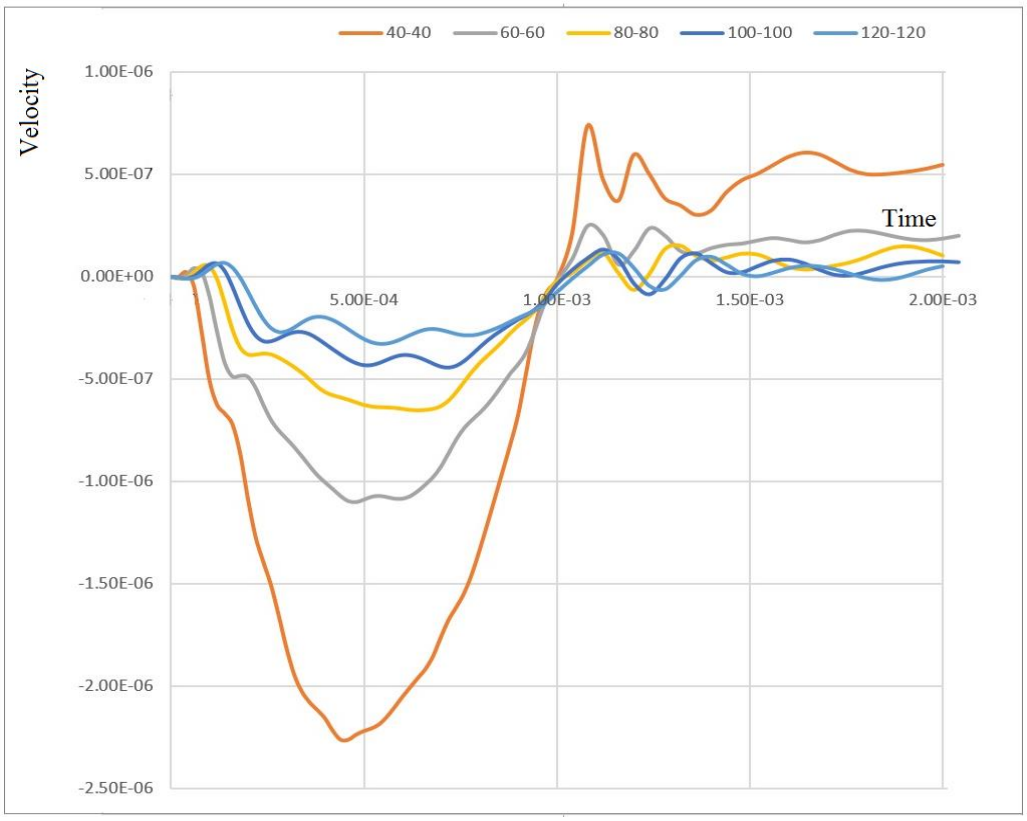

Figure (4.16): Velocity Response for Piles 40-60-80-100-120 cm Diameter Through Initial Parabola.

4.1.6 Discussion for Pile Case

Concrete piles with and without defects under sinusoidal impact force with half kilo hertz frequency are studied using the finite element analysis software ADINA. The following summary is obtained from the pile study:

There is an important zone of the velocity time history graph of the studied piles. This zone increases downward when the pile diameter decreases, or when the necking size increases for piles necked at their lower, middle, and upper parts. In addition, there is a similar time shift on the velocity time history diagram when the location of the necking moves from the pile top to the pile middle or the pile bottom. The distances between zones (Q), (P) and (O) are equal to the physical distances between the necking zones along the pile length.

A new schematic diagram with details concerning the necking location and volume is identified. The introduced schematic diagram shows an initial parabola and a successive one. These two parabolas are the most significant ones along the solution time, as the damping tend to affect other parabolas along the pile length.

For smaller pile diameters, the bottom of the parabola in the velocity time history graph is smoother with less noise meaning that the applied force fit well with smaller diameter piles than the larger ones.

For intact piles, the distance between the peak of the initial parabolas and the successive one on the time domain is equivalent to the pile length when it is multiplied by half of the wave velocity.

The ratio between the time difference along the peaks of the two initial parabolas, to the supposed travel time for an intact pile, is proportional to the ratio between the distance along the pile top to the necking zone, and the pile length. This relation could allocate the necking location along the pile length.

The ratio between the time indicating the distance between the pile head and the upper necking zone and the time indicating the pile length is the same as the ratio between the time indicating distance between the first parabola and the total pile length in the intact pile. Moreover, the ratio between the necking diameter to the pile diameter values, is proportional to the ratio between the velocity value of the second parabola peak in the necked pile to the velocity value of the second one at the intact pile. The necking diameter also can be deduced from this mentioned ratio.

4.2 Shallow Foundation Model

Numerical analysis is performed for shallow foundation to find the response of the impact pulse induced at its center. ADINA introduces time history for displacement, velocities and accelerations at any node for any degree of freedom there in the solved model. Time history for velocity is mandatory for simulating pile integrity test. Nodes selected for velocity-time history response is at fixed locations. Pulse location is assumed to be the origin. Nodes selected for introducing velocity responses where all located at three main axes. Ten models have been solved each with a specific defect location. These ten scenarios have been studied for velocity responses at specific nodes. Time solution are equal in all scenarios to maintain the domain length for all the graphs.

4.2.1 Main Model

The main model for the research is a cylinder of 3 meters diameter and 100 cm depth. A circular footing surrounded by a circular shaped cylinder of soil. An impact force is applied on the top center of the footing. The pulse of the impact force has the same frequency of a pile integrity test pulse, also impact duration. Although the pile integrity test is designed for long prismatic element like piles, as its pulse is subsonic or infra sonic, the target of the research is how to utilize the same subsonic pulse on a circular plate like a circular concrete footing. The values of the engineering and mechanical parameters are discussed.

4.2.2 Time Domain and Time Step Size

Time domain for all models or scenarios was 70 Millie seconds (7 x 10^{-4} sec.), it was divided to 140 steps, each of 5 micro seconds (5 x 10^{-6} sec.). The pulse induction frequency due to the applied impact force is

half kilo hertz, means for a one complete half sign wave as shown in Figure (4-17), the time domain is one millisecond. Table (4-3) introduces velocities of two corresponding nodes that will be explained latter, but it must be noted that the values of the velocities are so close at the same equal time intervals along the solution time domain. The table also shows three different intervals.

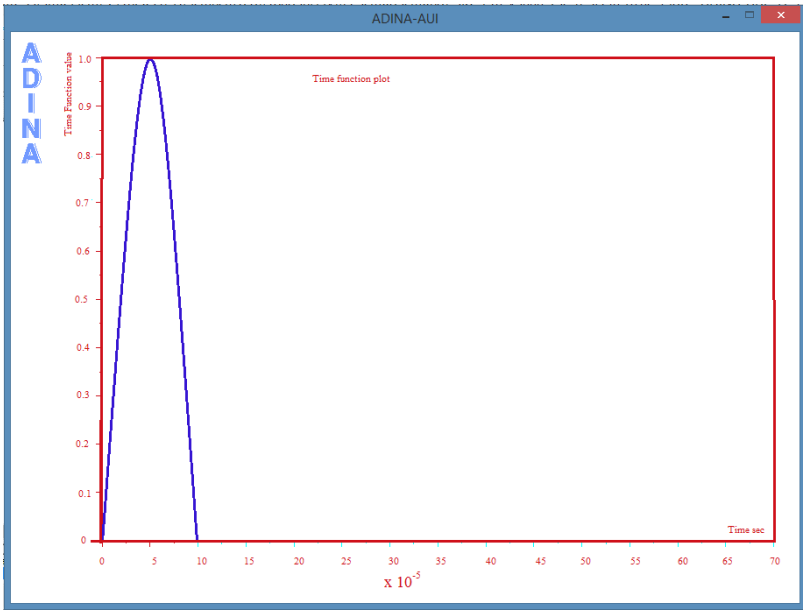

Figure (4.17): Impact force applied at center of foundation surface.

4.2.3 Rayleigh Damping

The damping defined in the modeling is Rayleigh damping, for the concrete stiffness only, and it is assumed by 70 x 10^{-7}. The assumption of the value is decided after many trial runs for several models. The main reason for such study, that while applying values recorded in other researches, the noise along the time history has vanished. The response pattern is mandatory and the backbone of the research. The decided value is an optimum that gives a reasonable velocity time response along the running time. Damping factor for concrete mass also damping factor soil mass and stiffness factor is assumed equal zero.

4.2.4 Soil and Concrete Grouping

Since ADINA is a finite element software, the model must be grouped into separate groups if they are from different materials. The model is of two groups, concrete group for circular footing and soil group surrounding it. Each one has its engineering property and its mechanical characteristics which will be declared latter.

4.2.5 Meshing

Meshing the model is the hardest part in the research, it takes many runs to find the optimum mesh and element size. In three dimensions, depth, traces and sectors. Probabilities to find the three parameters to give a reasonable velocity time response, with several runs are the longest and time consuming all over the research. The final and the optimum mesh is 3 cm for depth, 6 degrees for sectors and 1.5 cm for traces.

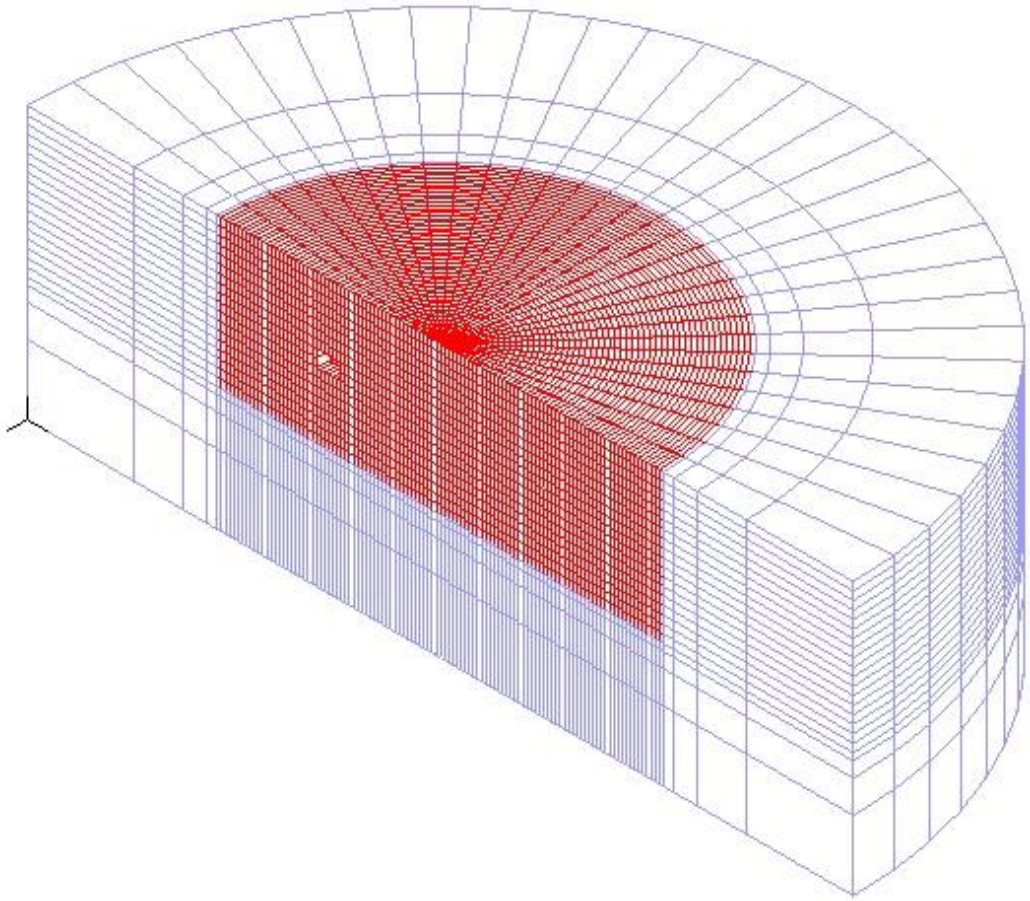

Figure (4.18): Shallow foundation model showing meshing.

4.2.6 Material Specifications

Assumption for material specification values has passed through several runs, as it effects on the main property the velocity, the velocity of the wave along the concrete is in terms of its elastic modulus and density. Elastic modulus of concrete is assumed as 2.25 kN/mm^2, its density is 25 kN/m^3 and its Poisson's ratio is 0.2. Soil is modeled using Mohr_Coulomb model. Poisson's ratio is 0.3, density is 19 kN/m^3 and friction angle is 40 degrees.

4.2.7 Parametric Study for Shallow Foundation

Parametric study is done through modeling ten models. The models are scenarios for the probability of the defect location plus. A healthy model (without defects) is also solved. Nine probabilities for nine defect locations are solved. The nine locations are at three levels from the top of footing level, and at three horizontal distances from the footing center, as shown in the Figures (4-19) and (4-20).

Table (4.3): Location of upper right corner of the defect relative to the pulse location

Scenario	1	2	3	4	5	6	7	8	9
Horizontal	0.36	0.135	0.585	0.135	0.585	0.135	0.585	0.36	0.36
Depth	0.24	0.09	0.39	0.39	0.09	0.24	0.24	0.39	0.09

4.2.8 Sensor's Locations

Sensor's location means the node at which the velocity time response is evaluated. Each run for a specified scenario for sure introduces a velocity time history at each node. Deciding specific locations must be reasonable or applicable at the real-life application. Though, the locations must be decided according to a rule. Locations for sensors in the research is related to a fixed value, which is the footing depth. Quarter the depth, half, three quarter and full depth value are the decided locations for the sensors, as shown in Figure (4.19). Each sensor has a corresponding one, as the defect is located in a half side, named as the defected half. The footing has two halves, defected and healthy, main sensor on the defected one and its corresponding on the healthy side. Also, three axes are considered, (0-180) axis is the main axis, passes through the impact and directly over the defect as shown in the Figure (4.22). (30-150) is an axis inclined to the main by 30 degrees. (60-120) is also an axis inclined to the main one by 60 degrees. (90-270) axis is not considered as it is a symmetrical axis and will gives two similar results for the velocity time history for the main sensor and its corresponding one. Figure (4.19) declares the difference between the three axes through the point of reflection and path of wave.

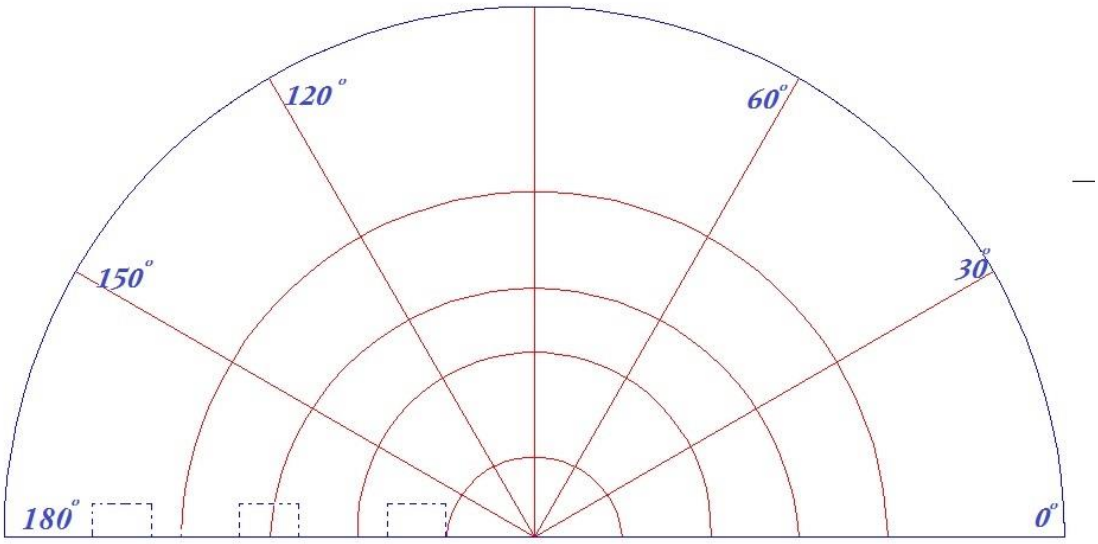

Figure (4.19): Semi plane view for footing declaring sensor's location

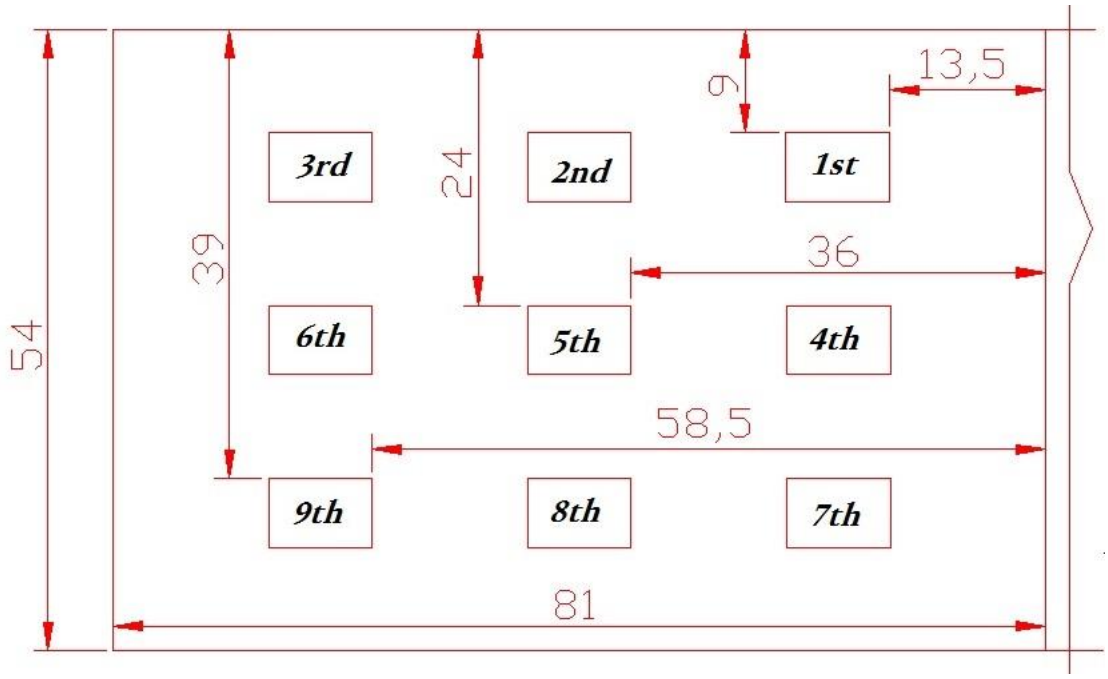

Figure (4.20): Section in defected half showing scenarios of defects.

4.2.9 Physical Peak Versus Graphical Peak

Using ADINA as a simulator for the real case, sure will not give the real-life values for the velocity time history, there is always a shift between the real and the model. Results obtained from ADINA in the

form of a schedule time versus velocity. Using excel to graph the output results is a foundation for the research to evaluate the methodology. However, calculating the physical time or the accurate time value, is a must to compare between the modeling value and the physical value. Table (4.4) is used 108 times for every scenario at every sensor location. Figure (4.21), shows a difference between the two couple of sensors at trace 13.5 cm for the fifth scenario. As shown there is a difference between the physical and the graphical time value, which will be discussed latter as errors histograms.

Table 4.4 shows the data of the fifth scenario with the d/4 sensor

Sensor h	0.135	velocity	3000
Sensor g	180	Physical time	2.54E-04
Defect H	0.36	Graph time	2.35E-04
Defect D	0.24	error	-8.04%
DT	1.0966193	Filter	10%
dt	0.76165000		

- Dt: refer to Figure (4-21), its equal (c + d).
- dt: refer to Figure (4-21), its equal (a+ b).
- Sensor h: surface distance between sensor and footing center.
- Sensor g: axis directed angle due to local cartesian co-ordinate.
- Defect H: surface distance between footing center and defect surface projection.
- Defect D: depth of defect from surface.

- Velocity: mechanical velocity from formula $\sqrt{\frac{E}{\rho}}$
- Physical time: equals V/ geometric distance.
- Graph time: first peak after applying 10% filter to the graph.

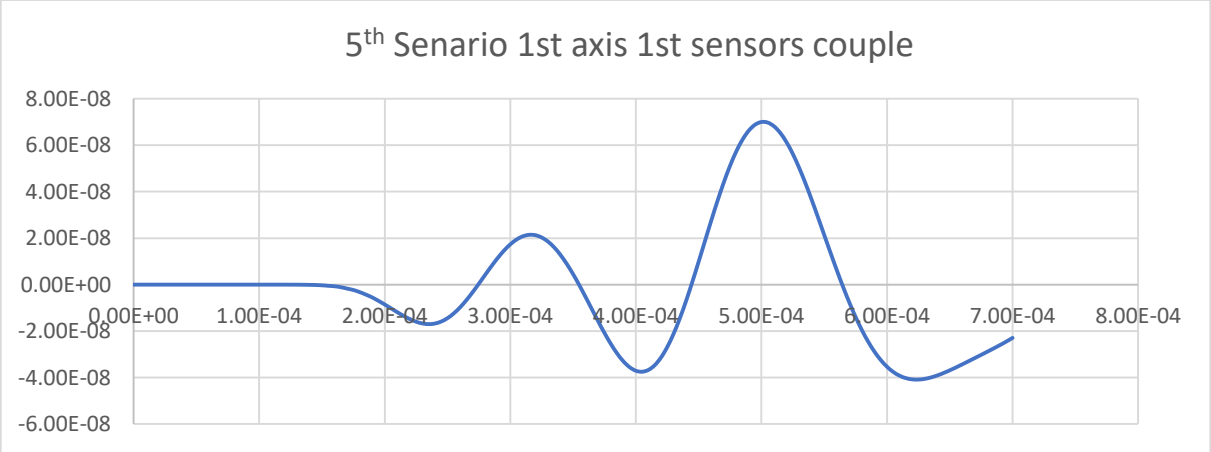

Figure (4.21): Velocity difference at fifth scenario for first couple sensors on first axis

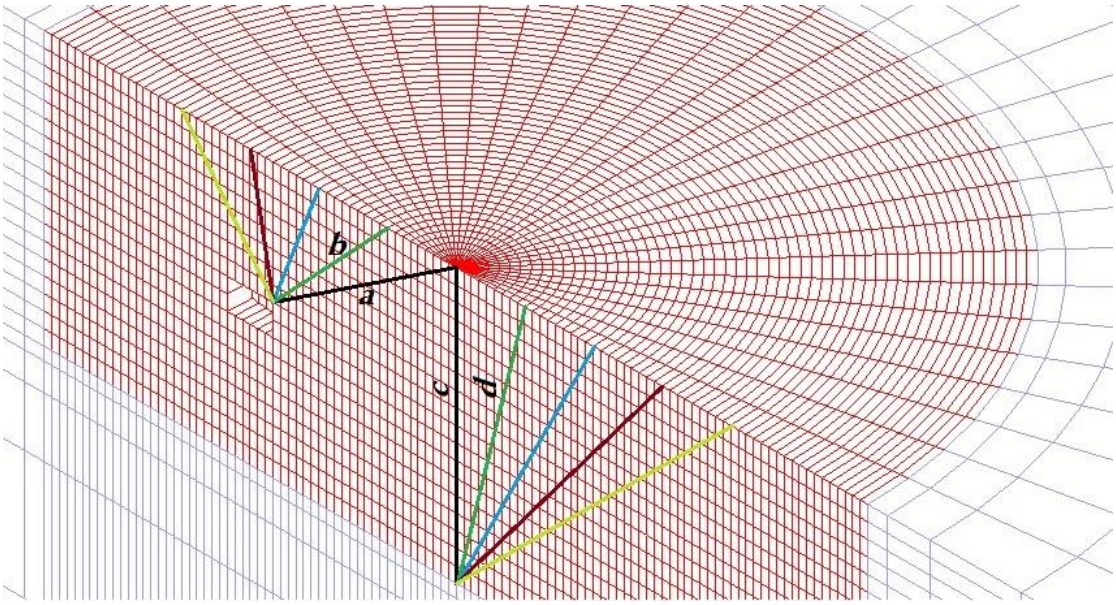

Figure (4.22): Section in defected half showing 180o axis for main sensors and their corresponding's.

4.2.10 Methodology

The Methodology for utilizing infra sonic wave at shallow foundation, is an algorithm based on an idea. The idea is comparison between two velocity responses, one in the healthy side and the other in the defected half. The comparison is done by applying two accelerometers where, both with the impact force or the footing center are all on the same straight line as shown in Figure (4.22). At least, there must be used six accelerometers, distributed in three couples, making three axes, falling in one circle, the circle center is the footing center or the impact location. The reading for the accelerometer is the velocity time response, the response value for each couple will be subtracted to give another graph. Three graphs, in each one of the three, the target value is the initial significant peak, which will be used to allocate the flaw location using code. Figures (4.23) and (4.24) show velocity time history, velocity on Y-axis and time on x-axis. Note that the difference can be barely noticed as the difference is insignificant. Figure (4.25) is the subtraction of the previous couple and is the research target, which the initial significant peak is deduced.

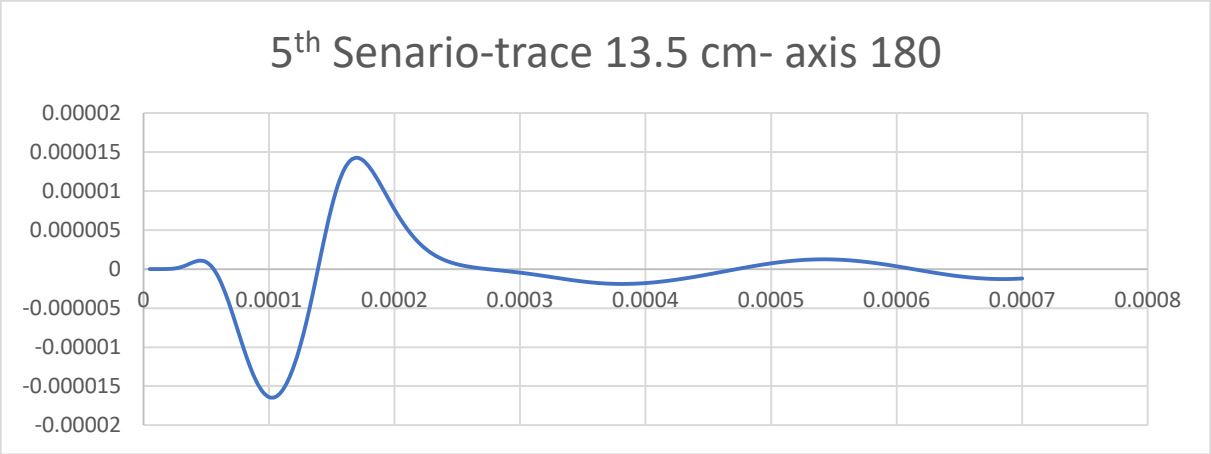

Figure (4.23) Velocity Response-Fifth Case-First sensor-axis 180o

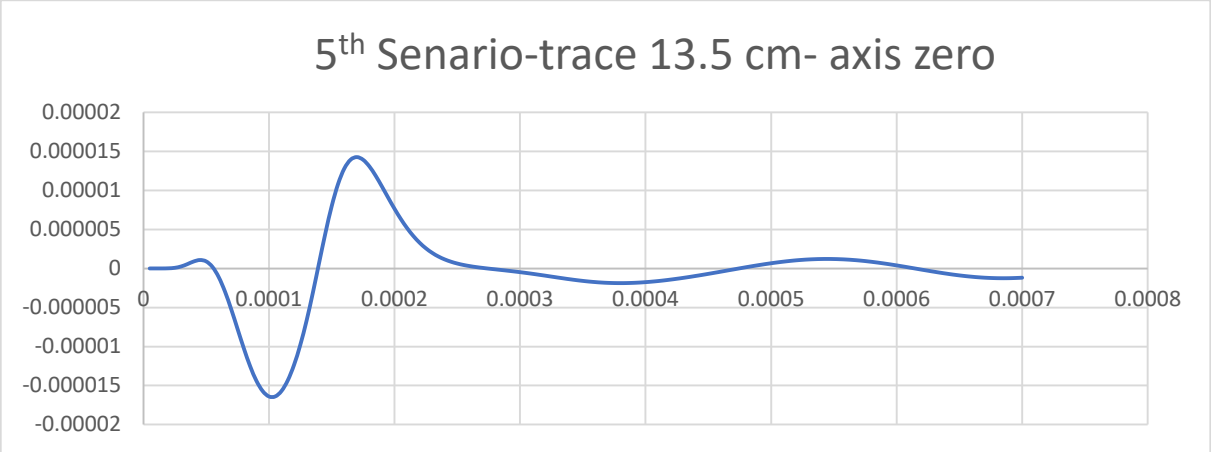

Figure (4.24) Velocity Response-Fifth Case-First sensor-axis zeroo

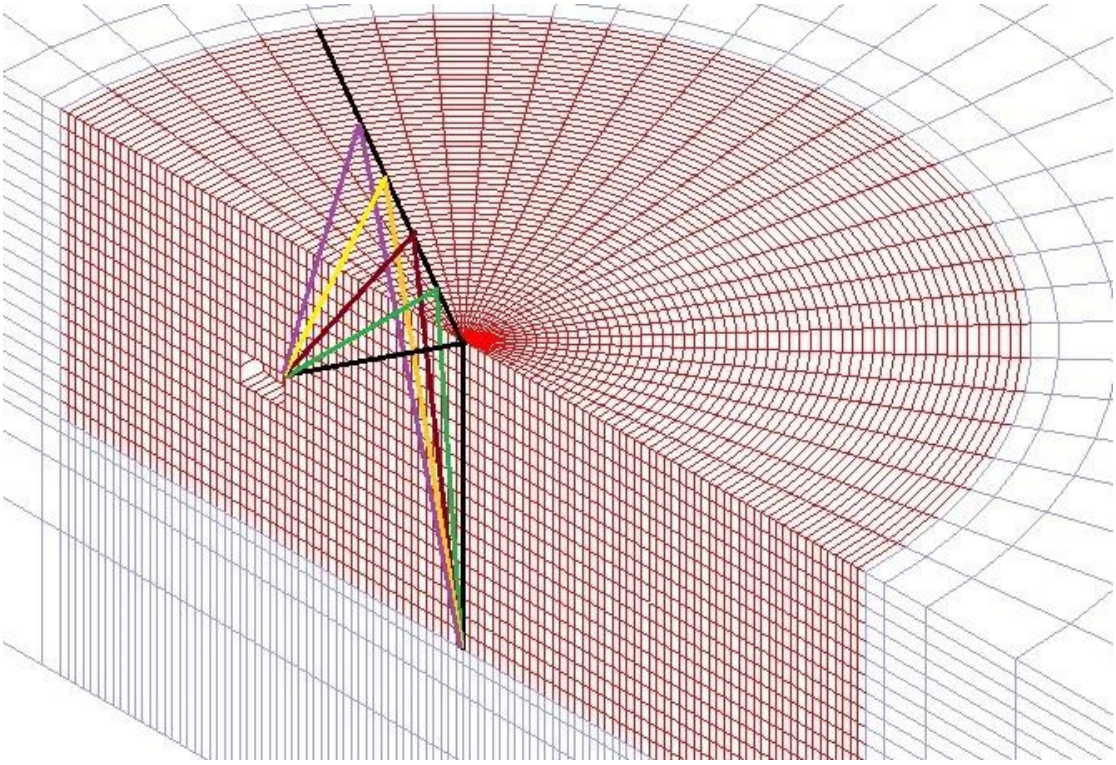

Figure (4.25): Section in defected half showing 150o axis for main sensors and reflections.

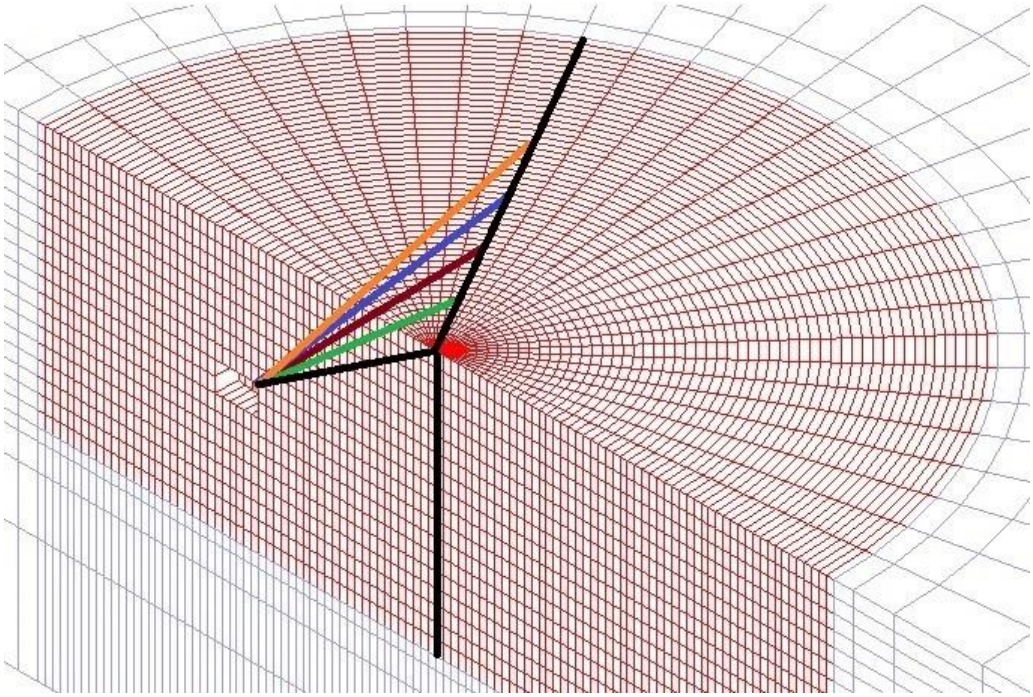

Figure (4.26): Section in defected half showing 120o axis for main sensors and reflections.

4.2.11 MATLAB Analysis

Deducing three values of time on three different locations is the main step to allocate the defect value, the idea is based on the unique probability for the wave path, this requires a MATLAB code, as it shown in the appendix.

4.2.12 Discussion of the Histograms

As discussed, the defects have nine scenarios, the sensors are distributed along three axes and around four traces. However, an error is found between the time value as been expected through physical formulas versus time value emerging from curves of velocity time history. The errors are found at all values, the observation which claims a discussion and analysis, and it will be clarified herein later.

4.2.12.1 First Scenario Histogram

The blue bars refer to sensors at traces of 13.5 cm radius, the red ones refer to 27 cm radius, the greens to 40.5 cm and the purples to 54 cm or the depth values.

As it clear, the errors are the highest for 180^{o} axis and 150^{o} at d/4 trace sensor or 13.5 cm radius, this is due to a reasons, that the sensor is so close to the impact force at which a surface wave can reach the sensor rapidly than the reflected wave from the defect. However, the sensor at axis 120 with the same radius its error is very low, due to the distance between the defect and the sensor (120^{o}–d/4) is longer than the distance between the defect and the other two sensors (180^{o}-d/4) and (150^{o}-d/4). The conclusion shows that, as the distance increases from the defect and the sensor as the noise decrease as the 10% filter is effective and reasonable.

The reds show an unexpected trend as it starts by approximately 17% then decreased to approximately 9.5% then increased to approximately 37.5%. The trend is different due to the phenomena of the in phase and the out phase for the reflected waves. It has no meaning to be explained through the geometric and mechanical boundaries.

The greens and the purples show a trend, as the angle increases as the error decreases. The sensors for the greens are (180^{o}_3d/4), (150^{o}_3d/4) and (120^{o}_3d/4), and for the purples are (180^{o}_d), (150^{o}_d) and (120^{o}_d). By another meaning, as the distance increase from the defect to the sensor as the error decreases and the filter is applicable.

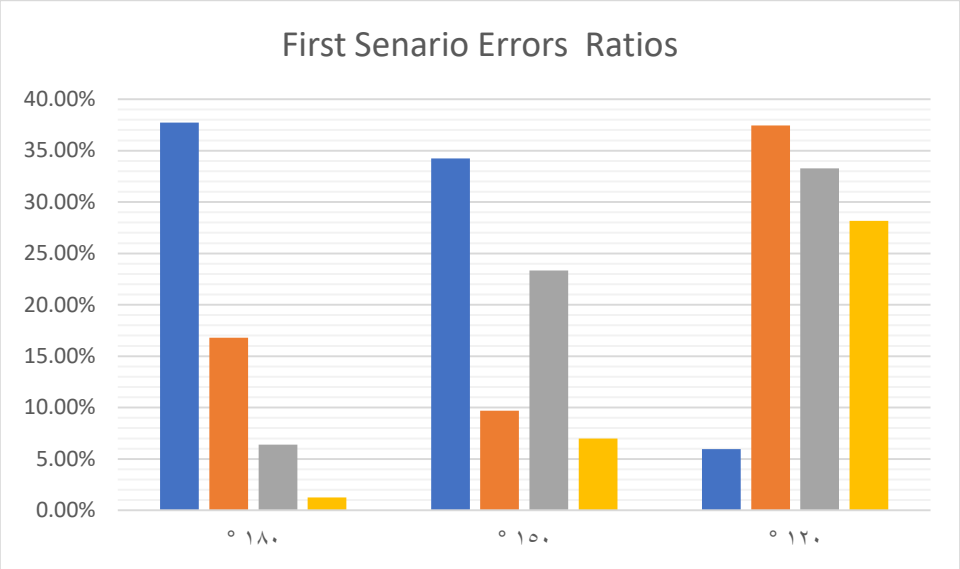

Figure (4.27): Histogram shows errors for first scenario at each sensor.

4.2.12.2 Second Scenario Histogram

From the shown histogram, the first observation is that the error is equal in all the traces of the axis 120^{o}, and the reason is simple, the distance between the defect and all sensors along the axis is almost so close, that no distinguished difference can be raised. All the bars are of a high value error except (180^{o}_d) sensor, and errors have an interval from mainly 15% to 30%. This interval shows that, surface defect at the distance equals to all sensors along the axis, has a property of a relative high error, if it's deduced through the research methodology. There is no significant trend for the sensors, either along an axis or around a trace.

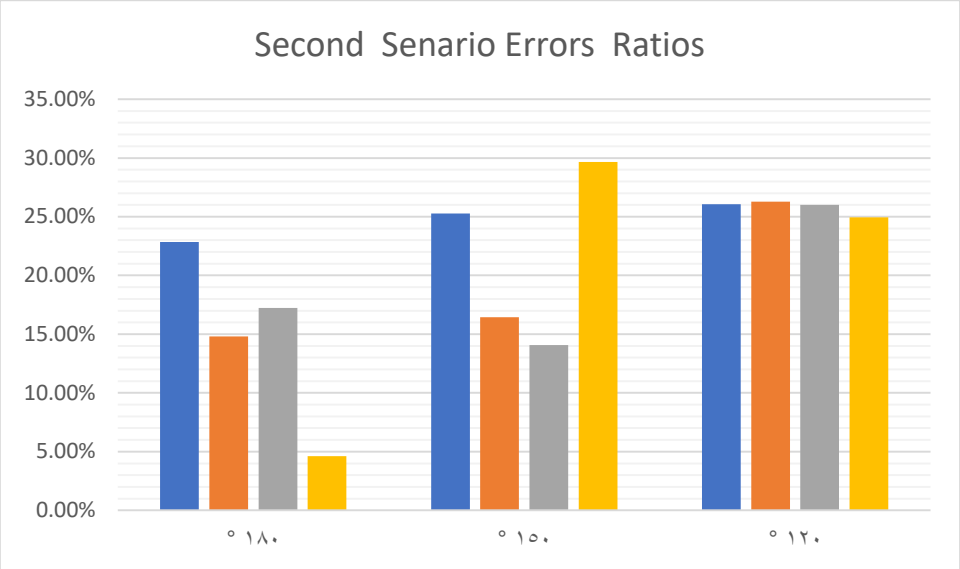

Figure (4.28): Histogram shows errors for second scenario at each sensor.

4.2.12.3 Third Scenario Histogram

The third crack exists close to the surface and far from the impact force, closer to the footing edge. As shown at the bar chart, the errors are mostly equal except the four sensors (180^o_3d/4), (180^o_d), (120^o_3d/4) and (120^o_d). All other readings within range from 23% to 28%. This gives a conclusion that, as the crack goes closer to the surface, and the sensors beyond the crack or between it and the impact point, the error is within previous range. However, the rule is excepted for those four values, so I return back to the excel to read the velocity time history and figuring out the reason. There found the target peak, but the program doesn't point it or choose it, instead, it chooses the next one, the reason is that the equations work with respect to the longest peak, I change the filter to 7% and it chooses the peak, at which all the errors will be with the same range with no un expected values.

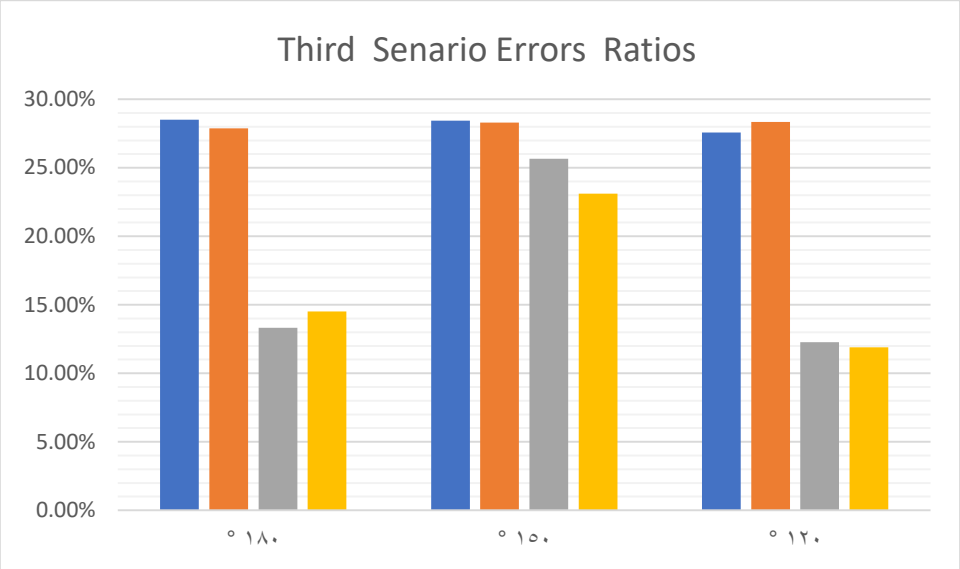

Figure (4.29): Histogram shows errors for third scenario at each sensor.

4.2.12.4 Forth scenario histogram

The fourth defect is at depth 24 cm and 13.5 cm horizontal distance from the surface center. The errors are reasonable and acceptable as it all comes below 10 %. Though, the measured nodes at trace 27 cm radius have a higher value, it may be due to that, the far edge of the defect is close to the trace 27 cm, which may cause noise and effect on the filtration.

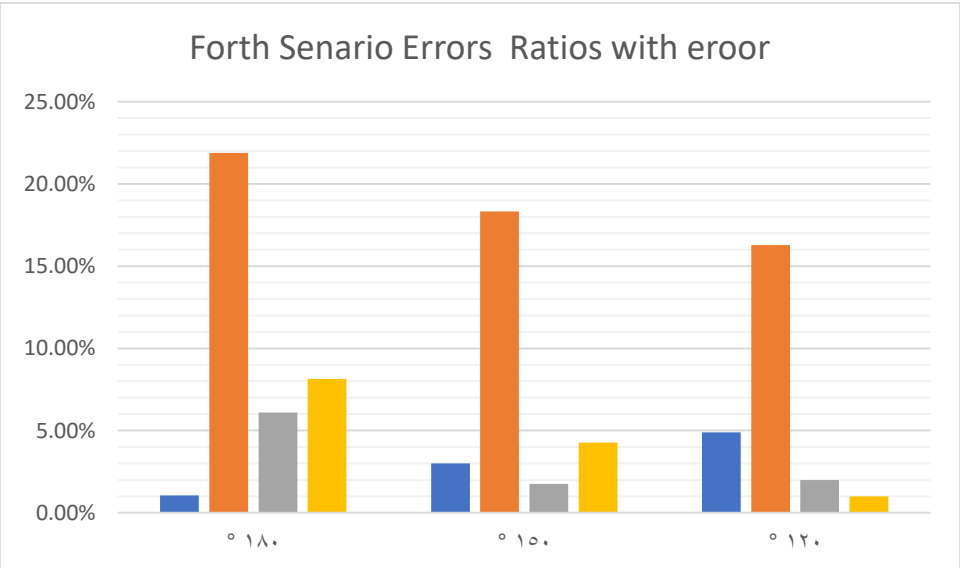

Figure (4.30): Histogram shows errors for fourth scenario at each sensor.

4.2.12.5 Fifth scenario histogram

The fifth defect is the middle defect, means it has equal distances between the left sensors and the right ones. Being in a central location gives a property for the equality, and that appears in the bar chart for axis 180^{o} and 150^{o}, both has low reasonable errors and also the two sensors (120^{o}_d/4) and (120^{o}_d/2) are also acceptable. For the other two sensors (120^{o}_3d/4) and (120^{o}_d), the errors is relatively high as the distance from the footing edge to these nodes is closer than the distance from the defect edge to the same nodes or sensors. The edge location will be so effective in the errors result as shown.

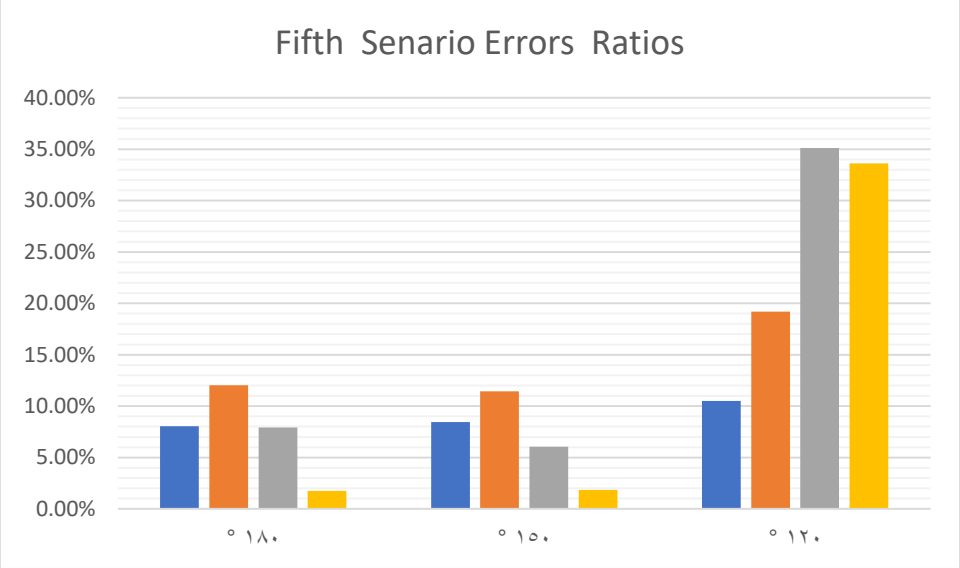

Figure (4.31): Histogram shows errors for fifth scenario at each sensor.

4.2.12.6 Sixth Scenario Histogram

The sixth defect is the far distance in the middle layer of defects, means all sensors are beyond it or all are between it and the impact location. The defect edge is closer to trace 54 cm radius and trace 40.5 cm trace than the edge or the bottom of the footing. High error values for 13.5 cm radius trace is due to the close distance between the impact

location and the 13.5 trace, that let the surface wave will reach closer more than one time, before the reflecting wave from the sixth scenario reaches the sensor node.

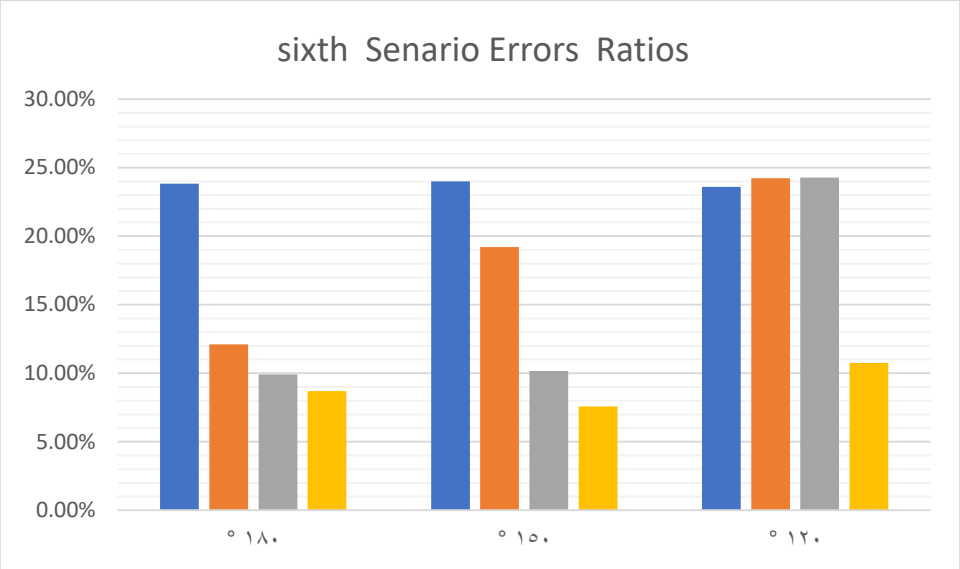

Figure (4.32): Histogram shows errors for sixth scenario at each sensor.

4.2.12.7 Seventh Scenario histogram

The seventh scenario, as shown in the bar chart, has a significant great observation. All values of the same color are equal, which means all sensors around the traces have the same error values. The errors are very low at 54 cm radius trace, and this is great, also for 13.5 cm and 27 cm radius trace the errors are acceptable. The green bars have jump rather than others though its location beyond the purple nodes. The only reason that explains this, is an amplification takes place in the reflection from the footing bottom and the defect, and this lapping affects 40.5 cm trace rather than others.

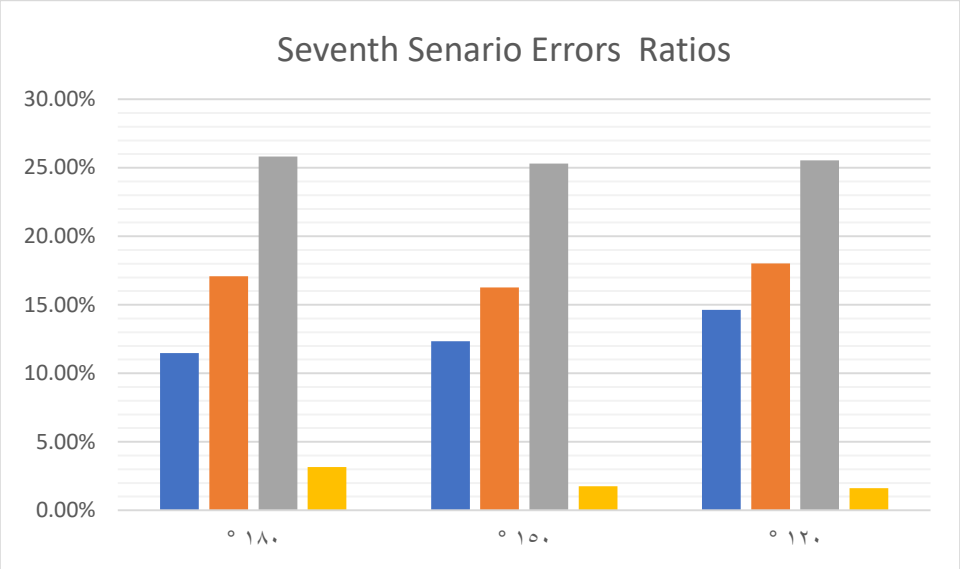

Figure (4.33): Histogram shows errors for seventh scenario at each sensor

4.2.12.8 Eighth Scenario Histogram

The eighth defect is closer to the footing bottom than the impact, and also not directly below the impact point, which gives this scenario particular importance than the seventh and the others. The majority of the bars is below 18% and which gives a good expectation to the location. As shown the beyond sensors (180^{o}_d) and (150^{o}_d) have the lowest values, and this is due to the previously clarified reasons, though it's not as in (120^{o}_d) since it is equal to 17%, which may be due to a tiny change required in the filter value.

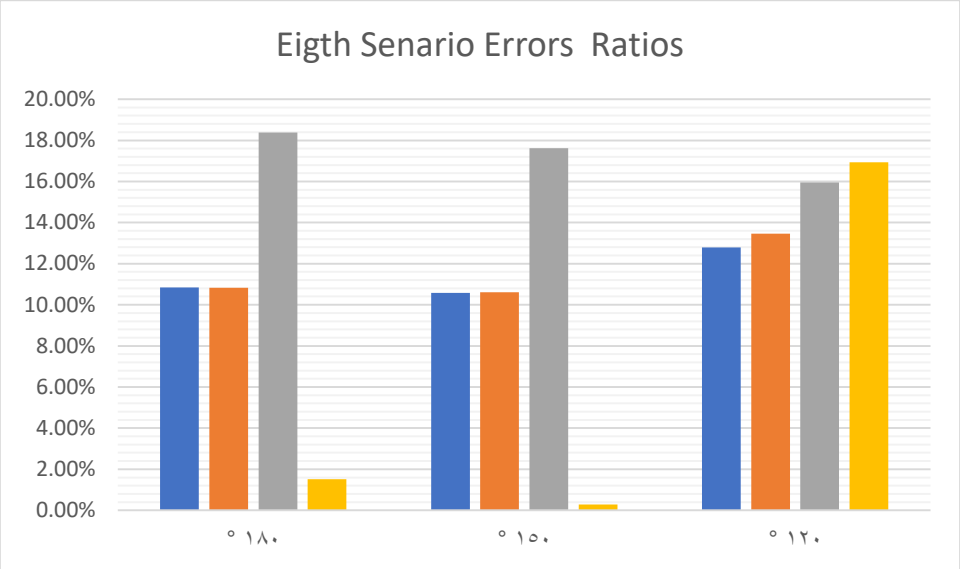

Figure (4.34): Histogram shows errors for eighth scenario at each sensor.

4.2.12.9 Ninth scenario histogram

The outmost and the last flaw may occur is the ninth, as it is the closest one to the edge and the bottom, and it is beyond all sensors. All these characteristics appear in the histogram. The trace of 180^{o} and 150^{o} is below 15%, which means as the axis in projected over the flaw or near its projection, as the error will be decreased. The 120^{o} has a relative high error than the previous, this due to the reflected wave from the edge may reach axis 120^{o} with no significant time delay versus the reflected wave from the defected.

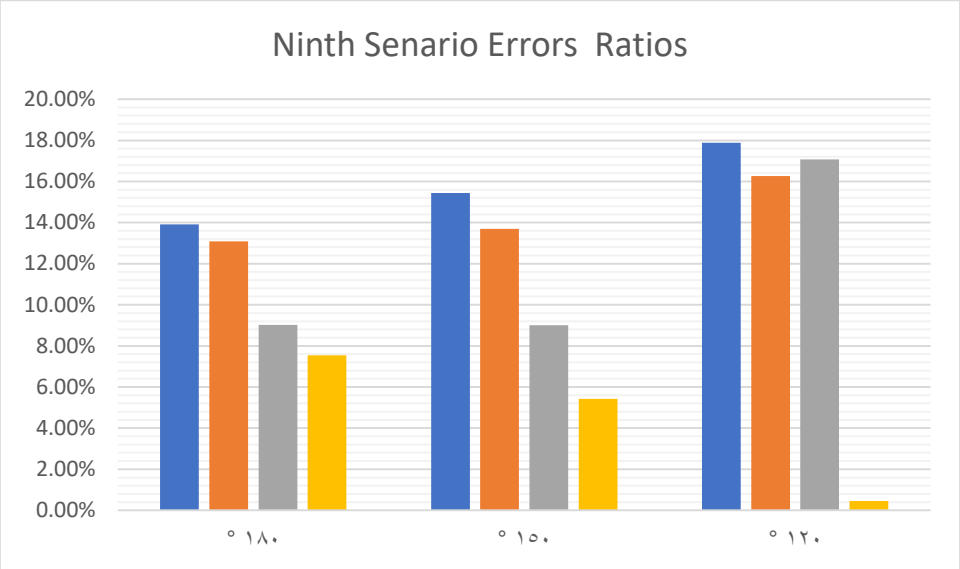

Figure (4.35): Histogram shows errors for ninth scenario at each sensor.

Chapter Five

Conclusions and Recommendations

Chapter Five

Conclusions and Recommendations

5.1 Introduction

Pile integrity test is a non-destructive test based on the principle of wave transfer from the pulse location to the pile end. As a non-destructive test, and a relatively low-cost test, both advantages encouraging to utilize the test to shallow foundations. Structure health monitoring is nowadays essential for concrete elements due to the probability of exciting cracks and honeycombs in any type of shallow foundations including isolated and raft foundations during concrete casting.

5.2 Conclusions

Based on the results of this research, the following conclusions are drawn:

1- Utilizing pile integrity test is an applicable methodology for structure health monitoring for deep and shallow foundations.
2- Frequency for pile integrity test may be not sufficient for generating waves capable to deduce cracks defect.
3- A simple rectification has to be added to the test by increasing the wave frequency, and this could be achieved by using a heavy metallic sharp egged hammer instead of the known pile integrity test.
4- The pile integrity test used at piles, required only one point for receiving wave, while for a shallow foundation, several points are required.

5- The number of hammer impacts required for the wave receiving points is depending on a simple estimation according to the footing depth and diameter.
6- Histograms of the error margins show that the maximum errors in the simulation is 40%, with an average error less than 15%. (This for pile or shallow foundations?).
7- For shallow foundations, the minimum errors is in case the defect is at seventh scenario with the sensor at distance equals the footing depth from the center. This shows that as the defect is directly under the pulse, deep or near the bottom, and the sensor it at the outer most circumference, this gives the best least errors.
8- At the first three scenarios the errors are relatively high and this may due to the surface waves transfer from the pulse to the sensors simultaneously with the reflected ones.
9- The fourth scenario is having the least errors referring for all sensors except the half depth location, and this may due to an inner phase for reflected waves from bottom and crack.

5.3 Recommendations for Future Work

The following topics are to be considered for further research:

1. Extending the research to various circular footing dimensions.
2. Extending the research to square and rectangular footings.
3. Extending research to double and triple defects.
4. Using a different methodology as modern optimization technique
5. Application for the case of real raft having several imbedded elements like sump and elevator pits and drainage networks.
6. Application of the method for the case of concrete initial hardening in massive rafts due to the lag between concrete truck supply and concrete pump cast.

References

[1]- Nazir, R., and El-Hussien, O. (2014). Mathematical Simulation of Pile Integrity Test (PIT). In 4th International Conference on Geotechnique, Construction Materials and Environment, Brisbane, Australia, Nov (pp. 19-21).

[2]- Wang, Y., Wang, K., Zha, Z., and Que, R. (2011). Soil-pile dynamic interaction in the viscous damping layered soils. The Open Civil Engineering Journal, 5(1).

[3]- Gao, L., Wang, K., Xiao, S., Li, Z., and Wu, J. (2016). An analytical solution for excited pile vibrations with variable section impedance in the time domain and its engineering application. Computers and Geotechnics, 73, 170-178.

[4]- Wu, J., Wang, K., and El Naggar, M. H. (2019). Dynamic response of a defect pile in layered soil subjected to longitudinal vibration in parallel seismic integrity testing. Soil Dynamics and Earthquake Engineering, 121, 168-178.

[5]- Gao, L., Wang, K., Wu, J., Xiao, S., and Wang, N. (2017). Analytical solution for the dynamic response of a pile with a variable-section interface in low-strain integrity testing. Journal of Sound and Vibration, 395, 328-340.

[6]- Shi, L., Xu, C., Cai, Y., and Geng, X. (2014). Dynamic impedances and free-field vibration analysis of pile groups in saturated ground. Journal of Sound and Vibration, 333(16), 3709-3731.

[7]- Jiang, J., Liu, D. J., Lu, Z. T., Tao, J., and Liu, H. X. (2014). A study on low strain integrity testing of platform-pile system using staggered grid finite difference method. Soil Dynamics and Earthquake Engineering, 67, 345-352.

[8]- Kuo, K. A., and Hunt, H. E. M. (2013). An efficient model for the dynamic behaviour of a single pile in viscoelastic soil. Journal of Sound and Vibration, 332(10), 2549-2561.

[9]- Wang, Z., Chen, L., and Xiao, Z. (2015). Quantitative analysis of low-strain characteristics on defective piles with constriction or segregation. The Open Civil Engineering Journal, 9(1).

[10]- Wang, Z. G., Chen, L., and Xiao, Z. C. (2013). Reflection waveform analysis of necking pile under low strain. The Electronic Journal of Geotechnical Engineering, 18, 5599-5609.

[11]- Cosic, M., Folic, B., and Folic, R. (2014). Numerical simulation of the pile integrity test on defected piles. Acta Geotechnica Slovenica, 11(2), 5-19.
[12]- Nazir, R., and El Hussien, O. (2015). Soil Damping Effects on Integrity Test of Piles. Jurnal Teknologi, 72(3).
[13]- Hou, S. W., Hu, S. J., Guo, S. P., and Zeng, Y. Q. (2016, February). The research of multi-defective piles for low strain testing and numerical simulation. In Structures Congress, 16º, Jeju Island (pp. 1-8).
[14]- Zhang, J., Liu, D. J., Geng, X., Gao, Z. J., Ke, Z. B., and Tao, J. (2016). Numerical analysis of low strain testing of 3-D axial symmetry viscoelastic pile–soil model. Indian Geotechnical Journal, 46(2), 175-182.
[15]- Ni, S. H., Isenhower, W. M., and Huang, Y. H. (2012). Continuous wavelet transform technique for low-strain integrity testing of deep drilled shafts. Journal of GeoEngineering, 7(3), 97-105.
[16]- Nazir, R. B., and El Hussien, O. (2015, June). Pile material and soil damping effects on Pile Integrity Test (PIT). In Testing and Measurement: Techniques and Applications: Proceedings of the 2015 International Conference on Testing and Measurement Techniques (TMTA 2015), 16-17 January 2015, Phuket Island, Thailand (pp. 101-106). CRC Press.
[17]- Likins, G., and Rausche, F. (2014). Pile damage prevention and assessment using dynamic monitoring and the beta method. In From Soil Behavior Fundamentals to Innovations in Geotechnical Engineering: Honoring Roy E. Olson (pp. 428-442).
[18]- De Jesus Souza, T., Hemsi, P. S., Aoki, P. C., and Valverde, R. M. (2017). Improvement and Extension of the Pile Integrity Test (PIT) under Existing Structures for Foundation Depth Evaluation. Two case studies in Brazil. Electronic Journal of Geotechnical Engineering, 22, 1003-1013.
[19]- Promputthangkoon, P., Swasdi, S., and Kuasakul, T. (2018). Interpretation of Pile Integrity Test Results Obtained from Model Concrete Piles Having Two Defect Locations. GEOMATE Journal, 15(47), 132-138.
[20]- Verbeek, G. E., and Middendorp, P. (2011). Determination of Pile Damage in concrete piles. DFI Journal-The Journal of the Deep Foundations Institute, 5(2), 44-50.
[21]- Lai, J., Yang, P. C., Yang, B. H., and Chang, D. W. (2017, June). Integrity testing of model pile with embedded accelerometers. In Proceedings 2017 International

Conference on Transportation Infrastructure and Materials, Qingdao, China (pp. 801-808).
[22]- Niederleithinger, E. (2012). Improvement and extension of the parallel seismic method for foundation depth measurement. Soils and foundations, 52(6), 1093-1101.
[23]- Abouhussien, A. A., and Hassan, A. A. (2017). Acoustic emission-based analysis of bond behavior of corroded reinforcement in existing concrete structures. Structural Control and Health Monitoring, 24(3), e1893.
[24]- Agrahari, J. K., and Kapuria, S. (2018). Active detection of block mass and notch-type damages in metallic plates using a refined time-reversed Lamb wave technique. Structural Control and Health Monitoring, 25(2), e2064.
[25]- Aryan, P., Kotousov, A., Ng, C. T., and Cazzolato, B. (2017). A model-based method for damage detection with guided waves. Structural Control and Health Monitoring, 24(3), e1884.
[26]- Berezovski, A., and Berezovski, M. (2017). Numerical simulation of acoustic emission during crack growth in 3-point bending test. Structural Control and Health Monitoring, 24(11), e1996.
[27]- Fang, Z., and Tse, P. W. (2018). Axial magnetized patch for efficient transduction of longitudinal guided wave and defect identification in concrete-covered pipe risers. Structural Control and Health Monitoring, 25(10), e2231.
[28]- Guan, R., Lu, Y., Duan, W., and Wang, X. (2017). Guided waves for damage identification in pipeline structures: A review. Structural Control and Health Monitoring, 24(11), e2007.
[29]- Li, F., Li, H., Qiu, J., and Meng, G. (2017). Guided wave propagation in H-beam and probability-based damage localization. Structural Control and Health Monitoring, 24(5), e1916.
[30]- Li, D., Tan, M., Zhang, S., and Ou, J. (2018). Stress corrosion damage evolution analysis and mechanism identification for prestressed steel strands using acoustic emission technique. Structural Control and Health Monitoring, 25(8), e2189.
[31]- Mokhtari, A. A., Ohadi, A., and Amindavar, H. (2017). Polygonal damage shape reconstruction in plates using guided Lamb wave. Structural Control and Health Monitoring, 24(5), e1907.

[32]- Guha, A., and Bijudas, C. R. (2018). Influence of modal characteristics of a partially debonded piezoelectric transducer in higher and subharmonic modes generated in Lamb wave. Structural Control and Health Monitoring, 25(10), e2239.
[33]- Qiu, J., Li, F., and Wang, J. (2017). Damage detection for high-speed train axle based on the propagation characteristics of guided waves. Structural Control and Health Monitoring, 24(3), e1891.
[34]- Sepehry, N., Asadi, S., Shamshirsaz, M., and Bakhtiari Nejad, F. (2018). A new model order reduction method based on global kernel k-means clustering: Application in health monitoring of plate using L amb wave propagation and impedance method. Structural Control and Health Monitoring, 25(9), e2211.
[35]- Serra, M., Festa, G., Vassallo, M., Zollo, A., Quattrone, A., and Ceravolo, R. (2017). Damage detection in elastic properties of masonry bridges using coda wave interferometry. Structural Control and Health Monitoring, 24(10), e1976.
[36]- Stojić, D., Nestorović, T., Marković, N., and Marjanović, M. (2018). Experimental and numerical research on damage localization in plate-like concrete structures using hybrid approach. Structural Control and Health Monitoring, 25(9), e2214.
[37]- Zhou, C., Zhang, C., Su, Z., Yue, X., Xiang, J., and Liu, G. (2017). Health monitoring of rail structures using guided waves and three-dimensional diagnostic imaging. Structural Control and Health Monitoring, 24(9), e1966.
[38]- Liao, S. T., and Roesset, J. M. (1997). Dynamic response of intact piles to impulse loads. International Journal for Numerical and Analytical Methods in Geomechanics, 21(4), 255-275.
[39]- Higgs, J. S., and Tongue, D. J. (1999). Advances in the use of the modified shock test system. Integrity Testing internal document.
[40]- Liao, S. T., Tong, J. H., Chen, C. H., and Wu, T. T. (2006). Numerical simulation and experimental study of parallel seismic test for piles. International Journal of Solids and Structures, 43(7-8), 2279-2298.
[41]- De Groot, P. H. (2014). The Parallel Seismic detection of defects in pile foundations.

[42]- Stepinski, T., Uhl, T., and Staszewski, W. (Eds.). (2013). Advanced structural damage detection: from theory to engineering applications.
[43]- ADINA, (2021). Automatic Dynamic Incremental Nonlinear Analysis Software, Version 9.70, ADINA R and D, Watertown, MA, USA.
[44]- Štrukelj, A., Pšunder, M., Vrecl-Kojc, H., and Trauner, L. (2009). Prediction of the Pile Behavior under Dynamic Loading Using Embedded Strain Sensor Technology, Acta Geotechnica Slovenica, 6, pp. 65-77.
[45]- Ding, X., Liu, H., Liu, J., and Chen, Y., (2011). Wave Propagation in a Pipe Pile for Low-Strain Integrity Testing, Journal for Engineering Mechanics, 137, 9, pp.598-609.
[46]- Li, Z. (2019). Torsional vibration of a large-diameter pipe pile embedded in inhomogeneous soil. Ocean Engineering, 172, pp. 737-758.
[47]- Wu, J. T., Wang, K. H., Gao, L., and Xiao, S. (2019). Study on longitudinal vibration of a pile with variable sectional acoustic impedance by integral transformation. Acta Geotechnica, 14(6), pp. 1857-1870.
[48]- Li, Z., and Gao, Y. (2019). Effects of inner soil on the vertical dynamic response of a pipe pile embedded in inhomogeneous soil. Journal of Sound and Vibration, 439, pp. 129-143.
[49]- Niederleithinger, E., (2006). Numerical Simulation of Non-Destructive Foundation Pile Tests, The 9th European Conference on NDT, Berlin, Germany.
[50]- Niederleithinger, E., (2008). Numerical Simulation of Low Strain Dynamic Pile Test, The 8th International Conference on the Application of Stress Wave Theory to Piles, Lisbon, Portugal, pp. 315-320.
[51]- Joram M. Amir, (2009). Pile Integrity Testing, Pile test.com, 1st edition.
[52]- Warrington, D., Wynn, R., (2000). Comparison of Numerical Methods to Closed-Form Solution for Wave Equation Analysis of Piling, The 13th Annual Meeting of the Tennessee Section of the American Society of Civil Engineers, Smyrna, USA.
[53]- Zhang, C., Yang, S., Zhang, J., and Xiao, N., (2010). The Numerical Simulation for the Low Strain Dynamic Integrity Testing and Its Application in Quality Diagnosis of Foundation Pile, Journal of Xiamen University (Natural Science), Xiamen, China.

Appendix

MATLAB code

```
ta=0.0005;tb=0.000489;tc=0.0004838;td=0.0004838;
xa=-0.0866;xb=-0.17;xc=-0.25;xd=-0.34641;ya=-0.05;yb=-0.1;yc=-
0.15;yd=-0.2;v=2828;
dta=ta*v;dtb=tb*v;dtc=tc*v;dtd=td*v;
Data=[];
for xi=-1:0.05:1;
   for yi=-1:0.05:1;
      for zi=0:0.05:0.6
         erora=dta-sqrt(xi^2+yi^2+zi^2)-sqrt((xa-xi)^2+(ya-yi)^2+zi^2);
         erorb=dtb-sqrt(xi^2+yi^2+zi^2)-sqrt((xb-xi)^2+(yb-yi)^2+zi^2);
         erorc=dtc-sqrt(xi^2+yi^2+zi^2)-sqrt((xc-xi)^2+(yc-yi)^2+zi^2);
         erord=dtd-sqrt(xi^2+yi^2+zi^2)-sqrt((xc-xi)^2+(yc-yi)^2+zi^2);
         erort=sqrt(erora^2+erorb^2+erorc^2+erord^2);
         Data=[Data;[xi yi zi erort]];
      end
   end
end
[n,m]=min(Data(:,4));
Data(m,1:3)
```

ملخص الرسالة

مقدمة :-

إن اختبار سلامة جسم الخازوق هو اختبار غير متلف يهدف إلى تقييم تجانس وصلابة خرسانة الخازوق المسلحة. وتتميز الاختبارات غير المتلفة عن باقى الاختبارات فى الحفاظ على جسم العنصر أو المنشأ الخرسانى قبل وبعد الاختبار. إن اختبار سلامة جسم الخازوق مبنِيٌّ على فكرة استحداث موجه داخل جسم الخازوق وتتبعها فى محاولة لاستكشاف وتحديد أماكن تواجد العيوب الخرسانية مثل الشروخ أو تغير القطاع. و قد حدث تطور فى هذا الاختبار لاستكشاف نوع أو شكل هذه العيوب. و لذا، فان فكرة انتشار الموجات داخل جسم الخازوق لتقييم سلامته وصلابة خرسانته المسلحه من الممكن أن تمتد لاستكشاف الشروخ الخرسانية داخل الأساسات السطحية.

أهداف البحث :-

يهدف البحث إلى ما يلى:-

1- استخدام نظرية عمل اختبار سلامة جسم الخازوق فى استكشاف عيوب و مشاكل الأساسات السطحية.
2- تطوير الاختبار نظريا لتحديد أماكن الشروخ والعيوب فى الأساسات السطحية.
3- شرح وتفسير الاشارات الموجية لاختبارات سلامة جسم الخازوق والرسومات الناتجة فى تحديد أماكن الشروخ والعيوب الخرسانية فى الأساسات السطحية.
4- تقديم طريقة لتصحيح القراءات الناتجة من اختبار سلامة الخازوق لنمذجة ومحاكاة تحديد العيوب فى خرسانة الأساسات السطحية.

خطة البحث

تـتـلخص خطوات البحث فيما يلى:

- استخدام برنامج العناصر المحدده ADINA فى نمذجة ومحاكاة تردد الموجات الاجهادية فى الخوازيق كجسم أو عنصر متجانس.
- تطوير فرضية الحل رقميا لـلـقواعد الخرسانية الدائرية كخطوة متقدمة من نتائج حل جسم الخازوق وأيضا تطويره كخطوة نهائية لاختبار شكل القواعد الخرسانية السطحية.
- تجميع قاعدة بيانات مما تم انجازه مصنفة حسب طبيعة الموجه على أساس نوع وأبعاد المادة التى يتم اختبارها

- دراسة التردد الموجى فى الخوازيق وتطوير الدراسة للقواعد السطحية تحت تأثير القوى الدورية بدالة جيبية و بدالة القوة الصدمية.
- دراسة التردد الموجى فى كلاً من جسم الخازوق السليم وما به شروخ وجسم القاعدة السطحية السليمة أو تلك التى بها شروخ.
- تقديم وجهة نظر لتحليل شكل الموجة التوافقية لكلاً من جسم الخازوق السليم وما به شروخ وتطوير طريقة تقييم القواعد السطحية فى حالتى وجود شروخ وبدون شروخ .

البحث فى ما يخص الجزء الخاص بالخازوق :-

تم دراسة الخوازيق علي قطاعات دائرية و منفذة بالكامل في التربة. تراوح أنصاف أقطارها من 40 إلى 120 سم ، وكلها لها نفس الطول 12 مترًا. يتم استخدام نموذج متماثل المحور في نمذجة الخازوق والتربة المحيطة ، حيث يساوي نصف قطر نموذج التربة 24 مترًا بالإضافة إلى قطر الخاوزق ، والارتفاع 24 مترًا. يتم استخدام نفس نمط العناصر في جميع النماذج التي لها نفس القيم. يُفترض أن تكون القيمة الصغيرة جدًا لعامل صلابة الاضمحلال من Raleigh $\beta = 70 \times 10^{-7}$ ، بينما يُفترض أن عامل كتلة التخميد α من Raleigh للركيزة يساوي صفرًا. بالإضافة إلى ذلك ، يعتبر عامل صلابة التخميد من Raleigh β وعامل الكتلة α للتربة = صفرًا. يتم اختيار هذه القيم الصغيرة جدًا بشكل أساسي نظرًا للمدة القصيرة جدًا لمراقبة موجة الحادث ، بحيث يُنظر إلى أن تأثير التخميد لن يؤثر على السلوك قبل فترة طويلة نسبيًا. الحمل الديناميكي المستخدم في هذا البحث هو حمل تأثير. تم تصميمه في برنامج ADINA كحمل مركّز يساوي 2.5 نيوتن مطبق على رأس الخازوق ، مع عامل الزمن. خطوات الحل المدروسة هي 50 خطوة خلال مدة النبضة التي تساوي 0.001 ثانية ، ثم 400 خطوة من 0.001 ثانية إلى 0.017 ثانية. وقت حمل الصدم هو 0.001 ثانية لموجة نصف جيبية وتردد 0.5 كيلو هرتز. تقسيم العناصر المحدوده جانبيا ورأسيا، له نفس الأبعاد. حجم العنصر داخل يساوي 5 سم في كلا الاتجاهين. تمت دراسة العلاقة بين الوقت والسرعة عند نقطة معينة لجميع الحالات. موقع النقطة المدروسة هو (3/1 * نصف قطر الخازوق) من مركزه. يتم دراسة موقع العيب في الخازوق في أماكن متعددة بما في ذلك قطر الخازوق وقطر العيب أو الاختناق والنسبة بينهما.

البحث فيما يخص الأساسات الضحلة :-

كان النطاق الزمني لجميع السيناريوهات 70 ملي ثانية (7×10^{-4} ثانية) ، تم تقسيمه إلى 140 خطوة ، كل منها 5 مايكرو ثانية (5×10^{-6} ثانية). التردد المستحث للنبضة بسبب قوة التأثير المطبقة هو نصف كيلو هرتز ، وهذا يعني نصف موجة كاملة .المجال الزمني هو ثانية ميل واحد. قيم السرعات قريبة جدًا في نفس الفترات الزمنية المتساوية على طول المجال الزمني للحل. التخميد المحدد في النمذجة هو تخميد Raleigh ، لصلابة الخرسانة فقط ، بفرض $70 \times 10\text{-}7$. تم تحديد افتراض القيمة بعد العديد من عمليات التشغيل لعدة نماذج. السبب الرئيسي لهذه الدراسة ، أنه أثناء تطبيق القيم المسجلة في أبحاث أخرى ، اختفت الضوضاء بطول محور الزمن . نمط العلاقة بين سرعة الموجه و الزمن هوالأساس و الركيزة الأساسية للبحث. القيمة المحددة هي القيمة المثلى التي تعطي استجابة زمنية معقولة للسرعة على طول وقت التشغيل. معامل الاضمحلال لكتلة الخرسانية و معامل الاضمحلال لكتلة التربة و صلابتها يفترض بصفر. يعد ربط النموذج أصعب جزء في البحث ، حيث يتطلب الأمر العديد من عمليات التشغيل للعثور على الشبكة المثلى ، كما أن ربط النموذج صعب للغاية لأنه يحتوي على ثلاثة أبعاد وعمق وآثار وقطاعات. تعد احتمالات مواءمة المعلمات الثلاثة لإعطاء استجابة زمنية بسرعة معقولة ، مع تشغيل عدة هي أطول وأصعب مهمة في جميع أنحاء البحث. الشبكة النهائية والمثلى هي 3 سم للعمق و 6 درجات للقطاعات و 1.5 سم للآثار. تم حل تسعة احتمالات لتسعة مواقع عيب. المواقع التسعة على ثلاثة مستويات من مستوى سطح القاعدة ، وثلاثة مسافات أفقية من مستوح سطح القاعدة. موقع المستشعر يعني النقطة التي يتم فيها تقييم استجابة وقت السرعة. كل سيناريو محدد يسجل وقت السرعة في كل نقطة. يجب أن يكون تحديد مواقع المستشعرات معقولًا أو قابلاً للتطبيق في التطبيق الواقعي.

جـــامـعـة الـزقـازيـق

كـلـيـة الـهـنـدسـة

قـسـم الـهـنـدسـة الإنـشـائـيـة

استخدام اختبار سلامة الخازوق فى اختبار الشروخ بالأساسات السطحية

رسالة مقدمة من

المهندس

عبدالله عليوه عبدالله الـمـسـلـمـى

بكاليوريوس الهندسة المدنية 2001

لـنـيـل درجة الماجستير

فى العلوم الهندسية

تخصص الهندسة الإنشائية

تحت اشراف

الأستاذ الدكتور طارق نجيب سالم

أستاذ هندسة الأساسات و ميكانيكا التربة

قسم هندسة الانشاءات

كلية الهندسة جامعة الزقازيق

الأستاذ الدكتور عاطف عراقى بكرى

أستاذ تحليل وميكانيكا الانشاءات

قسم هندسة الانشاءات

كلية الهندسة جامعة الزقازيق

2023